1   Numerical Prediction of $\{11\bar{2}2\}\langle11\bar{2}\bar{3}\rangle$ Compression Twin Activation

2   in Commercially Pure Titanium under Uniaxial Tension

3

4   Yoshiki Kawano [a,1], Masatoshi Mitsuhara [b,2], Tsuyoshi Mayama [c,3],

5   Misaki Deguchi [b,4], Zishuo Song [b,5]

6

7   [a] Faculty of Engineering, Kitami Institute of Technology, Kitami 090-8507, Japan

8   [b] Department of Advanced Materials Science and Engineering, Faculty of Engineering

9   Sciences, Kyushu University, Fukuoka 816-8580, Japan

10 [c] Department of Materials Science and Engineering, Faculty of Engineering, Magnesium

11 Research Center, Kumamoto University, Kumamoto 850-8555, Japan

12

13 [1] kawano_y@mail.kitami-it.ac.jp

14 [2] mitsuhara@kyudai.jp

15 [3] mayama@kumamoto-u.ac.jp

16 [4] deguchi.misaki.004@s.kyushu-u.ac.jp

17 [5] song.zishuo.602@s.kyushu-u.ac.jp

18

19

20

21

Highlights

1. $\{11\bar{2}2\}$ compression twinning was the dominant system under a uniaxial tensile test of commercially pure titanium with RD-split texture.

2. Deformation in the microstructure was successfully reproduced by crystal plasticity analyses and slip operation factor calculations.

3. Criterion using hydrostatic pressure and resolved shear stress helped predict the twinning positions with high accuracy.

1 **Abstract**

2 In this study, the criteria for $\{11\bar{2}2\}$ compression twinning in commercially pure

3 titanium (CP-Ti) were investigated by uniaxial tensile tests, crystal plasticity finite

4 element (CPFE) analyses, and slip operation factor (SOF) calculations. First, the

5 aggregates of the [0001] axes of CP-Ti were inclined in the rolling direction (RD),

6 implying its RD-split texture. The development of the crystal orientation distribution with

7 deformation was observed by electron back-scattered diffraction (EBSD). Active slip

8 systems were identified by kernel average misorientation (KAM) and intergranular

9 misorientation axis (IGMA) analyses. The dominant slip system was prismatic <a>,

10 whereas the non-prismatic <a> slip systems were activated near the grain boundary.

11 Active twin systems were also identified by the rotation angles of the [0001] axes between

12 the twin and matrix. The dominant active twin system was the $\{11\bar{2}2\}$ compression twin,

13 although a uniaxial tensile load was applied. Second, the positions of $\{11\bar{2}2\}$ twinning

14 were predicted by CPFE analysis using the resolved shear stress (RSS) criterion while

15 considering plastic deformation. SOF analysis was also employed for the prediction. The

16 CPFE and SOF analyses yielded almost the same level of prediction accuracy. However,

17 these calculations do not completely predict the twinning positions. Finally, the criteria

18 for $\{11\bar{2}2\}$ twinning were discussed, and it was revealed that hydrostatic pressure and

1   RSS are possible criteria for $\{11\overline{2}2\}$ twinning in the continuum model.

2

3   Key words: CP-Ti; HCP; EBSD; twin; crystal plasticity; slip operation factor

4

5

6

7

8

9

10

11

12

13

14

15

16

17

18

1. Introduction

Commercially pure titanium (CP-Ti) has excellent corrosion resistance, and is high

demand in a wide range of fields such as chemical plants, power industry, and

automobiles [1]. Therefore, clarification of the deformation and fracture mechanisms

under room temperature environments will contribute to improving the safety and

performance of various products. The mechanical properties of CP-Ti with a hexagonal

close-packed (HCP) structure change with deformation modes, such as slip systems and

twin systems [2][3][4][5][6]. For example, twinning in CP-Ti affects the work hardening

rate [7][8] and fatigue fracture [9][10][11][12] of CP-Ti. However, criterion for twin

activation is not clear, and it is difficult to quantitatively evaluate the fatigue strength and

workability of CP-Ti in connection with twinning. Identifying the conditions under which

these deformation modes are activated provides a better understanding of the expression

mechanism of the mechanical characteristics and fracture behavior of specimens;

however, some points remain unclear.

The slip systems of CP-Ti are basal (Bsl<a>), prismatic <a> (Pri<a>), 1st-pyramidal <a>

(Pyr1<a>), 1st-pyramidal <c+a>, and 2nd-pyramidal <c+a> systems, while the mainly

1 observed twin systems are the tensile ones of $\{11\bar{2}1\}\langle11\bar{2}6\rangle$ and $\{10\bar{1}2\}\langle10\bar{1}\bar{1}\rangle$, and

2 the compression ones of $\{10\bar{1}1\}\langle10\bar{1}2\rangle$ and $\{11\bar{2}2\}\langle11\bar{2}3\rangle$ [13][14]. The individual

3 activities of these deformation modes depend on the manufacturing and loading

4 conditions [6][15], and thus, elucidating the relationship between these two has attracted

5 significant research attention [6].

6

7 Critical resolved shear stresses (CRSSs) dominate the activities of slip systems. The

8 CRSSs for CP-Ti are different from those reported previously [16][7][17][18]. The

9 activities of the slip systems in CP-Ti follow Schmid's law. Therefore, when the CRSSs

10 for individual slip systems are evaluated by experimental or numerical analysis, the

11 spatial distributions of strain can be obtained by numerical methods like crystal plasticity

12 finite element (CPFE) analysis. Numerical analyses contribute greatly to the detailed

13 understanding of the deformation mechanisms [17][19][20][21]. CPFE analysis

14 represents the deformation at the crystal grain level. In the full-field CPFE analysis, the

15 microstructure is considered, and the mechanical interactions among the grains are

16 naturally incorporated. Thus, the strain and stress concentrations induced by deformation

17 incompatibility are naturally represented [22][23][24]. In recent years, CPFE analysis has

18 been conducted using microstructural images obtained from electron back-scattered

diffraction (EBSD) patterns, and the predicted strain distributions and slip activities

correspond well with those obtained experimentally [19][20][21][25].

In contrast to the conditions of slip systems, prediction of twinning is difficult. To explain

the origin of twinning, a criterion is typically employed, in which twin systems are

activated when subjected to high resolved shear stress (RSS). Lebensohn and Tomé

(1993) reported that the activation of twinning can be correctly described by the Schmid

criterion of CRSS, independent of other stress components [26]. However, non-Schmid

behavior has been observed in twinning [15][27][28]. In metal materials, tensile and

compression twinning typically occur under tensile loading and compressive loading,

respectively. However, different results have been observed in CP-Ti with

crystallographic textures. Specifically, compression [29][30] and tensile twinning [31] are

observed under the tensile and compressive loading, respectively. However, the

mechanical criteria for the opposite twinning to the loading direction occurs are unknown.

Thus, the criteria for twinning remain an open discussion. Furthermore, other factors,

such as deformation incompatibility and accumulation of dislocations, have also been

reported to influence twinning [14][32]. Thus, the prediction of twinning in CP-Ti

requires that the deformations in individual grains be evaluated with a high degree of

1   accuracy.

2

3   Several crystallographic textures exist in α-Ti [33] and split textures, in which aggregates

4   of (0001) axes are split and inclined in the rolling direction (RD) or transverse direction

5   (TD), are typically formed in CP-Ti by the rolling process. When CP-Ti with split textures

6   is subjected to tensile loading, both compression twinning and tensile twinning can be

7   observed at high activity [30][29]. While this fact is well known, the mechanical criterion

8   for compression twinning under tensile deformation has not been investigated. One of the

9   purposes of this study was to reveal this criterion.

10

11   The macroscopic stress-strain relationships of CP-Ti were successfully reproduced by

12   crystal plasticity analysis using the Schmid factor criterion of CRSS while considering

13   twin deformation [34][35]. The prediction of twinning positions at the microscopic level

14   was also attempted. Lind et al. (2014) studied the distribution of the RSS for twins in a

15   polycrystalline CP-Ti in the elastic range, and the results showed that high-RSS regions

16   did not completely coincide with the experimentally observed twinning positions [36].

17   Yang et al. (2011) successfully reproduced a twinning position in a region consisting of

18   25 grains by accurately predicting slip strain distributions for individual slip systems

1   using crystal plasticity analysis [37]. These results indicate that the positions of

2   compression twinning can be accurately predicted by full-field-type crystal plasticity

3   analysis when the slip system activity is correctly predicted.

4

5   As stated above, the development of deformation incompatibility is an important factor

6   for twin activation. In other words, evaluation of the mechanical interaction between

7   grains is required to predict twinning. The slip operation factor (SOF), which is a function

8   of the Schmid factor and CRSS and considers the degree of mechanical interactions

9   between grains and their range, is an indicator to evaluate ease of slip operation. SOF not

10   only can reproduce the strain distributions of α-Ti in the initial deformation but also

11   estimate the range and degree of mechanical interaction between regions [38][39]. Kawano

12   et al. (2019), by using SOF, showed that the mechanical interaction range is longer in the loading

13   direction than that in the direction perpendicular to the loading direction [38]. Furthermore, Kawano

14   et al. (2021) succeeded in considering the secondary slip systems in the SOF [39]. If twinning is

15   predicted by the Schmid criterion of CRSS, the SOF method, which is simpler with lower calculational

16   cost, can also predict twinning. Then, the mechanical interaction range can also be estimated by SOF.

17

18   The objectives of this study are three-fold: i) understanding the criteria for twinning in

CP-Ti at room temperature, ii) predicting the twinning positions by SOF, and iii)

evaluating interaction range affecting twinning by SOF. First, a uniaxial tensile test of

CP-Ti was conducted. The changes in the crystal orientation distributions under tensile

deformation were observed using EBSD. The development of nonuniformity in crystal

orientation distributions and twinning positions, as well as the activated slip systems,

were experimentally determined. Second, the experimental crystal orientation

distributions were reproduced by CPFE analysis, and the twinning positions were

predicted. Estimation of the twinning positions induced by deformation incompatibility

requires the correct representation of the deformations in individual grains. Grain shapes

affect deformation more significantly than tuning finer parameters for the constitutive law

[40]. The geometric model for the CPFE analysis was built from the EBSD crystal

orientation maps, and a tensile deformation analysis was conducted. Next, the twinning

positions were estimated using the SOF. Finally, the criteria for twinning were discussed.

2. Experimental procedure

2.1 Material and tensile test condition

For this study, we used the same CP-Ti specimen as that used by Kawano et al. (2020)

[38]. Table 1 shows the chemical compositions of the specimens. The processing

1   sequence used for the specimen involved hot and cold rolling with heat treatment at

2   650 °C for 2 h to homogenize the microstructure. The CP-Ti plate formed by this rolling

3   process, with a thickness of 1 mm, was cut into the specimen's shape, as shown in Fig.

4   1a, by using an electric discharge machining. Wet polishing with emery papers and

5   buffing with diamond paste were conducted on the specimen, followed by

6   electropolishing to remove the work-affected layer on the surface.

7

8   Fig. 1 shows the EBSD orientation map plotted for the ND and the (0001) pole figure,

9   where the aggregates of the (0001) axes inclined in the RD and split, the so-called RD-

10   split texture, are depicted. The specimen was subjected to uniaxial tensile loading in the

11   RD, and the strain rate was 1.0×10^{-3} s^{-1}. The tensile test was conducted in a scanning

12   electron microscope (SEM) chamber, and in-situ EBSD measurements were performed.

13   In these EBSD measurements, the position of the crosshead in the tensile tester was

14   maintained, and the measurements were conducted after the plastic relaxation of the

15   specimen, i.e. once the stress stopped decreasing.

16

17   **2.2 Kernel average misorientation**

18   As shown in Fig. 2a, the kernel average misorientation (KAM) is calculated using two-

1   dimensional elements, (i, j), where each crystal orientation has been assigned to (i, j).

2   Each misorientation angle at element (i, j) is calculated using the misorientation angles

3   between the element (i, j) and the four neighboring elements. Thereafter, the average

4   of the four misorientation angles was assigned to the KAM in (i, j). The accuracy of

5   KAM can be increased by using a larger number of elements. However, as shown later,

6   clear KAM distributions could be obtained even under the calculation using the four

7   neighbor elements in this study.

8

9   The crystal orientation is expressed by the Euler angle (ϕ_1, Φ, ϕ_2) of the Bunge definition

10   [41]. The rotational relationship between the global and crystal lattice coordinate systems

11   was set to the state shown in Fig. 1b when $(\phi_1, \Phi, \phi_2) = (0, 0, 0)$. Three misorientations

12   were employed to accurately evaluate the differences in the activities of the slip systems:

13   (i) misorientation angle $\Delta\theta$ using typical KAM calculations, (ii) misorientation angles

14   $\Delta\phi$ around the [0001] axes (Fig. 2c), and (iii) $\Delta\Phi$, which correspond to the difference

15   in the inclination angles between the [0001] axes (Fig. 2d). Kernel average

16   misorientations calculated using $\Delta\theta$, $\Delta\phi$, and $\Delta\Phi$ are denoted as KAM, KAM_a, and

17   KAM_c, respectively. The calculation methods for $\Delta\theta$, $\Delta\phi$, and $\Delta\Phi$ are described

18   below.

1

2   For the calculation of $\Delta\theta$, the crystal orientations in (i,j) and (k,l) are expressed

3   as square matrices $\left[\mathbf{g}^{ij}\right]$ and $\left[\mathbf{g}^{kl}\right]$, and the misorientation, $\left[\Delta\mathbf{g}\right]$, between them is

4   calculated as follows:

5

6   $$\left[\Delta\mathbf{g}\right]=\left[\mathbf{g}^{ij}\right]^{-1}\left[\mathbf{g}^{kl}\right]=\left[\mathbf{g}^{ij}\right]^{T}\left[\mathbf{g}^{kl}\right]=\begin{bmatrix} g_{11} & g_{12} & g_{13} \\ g_{21} & g_{22} & g_{23} \\ g_{31} & g_{32} & g_{33} \end{bmatrix}. \qquad (1)$$

7

8   $\Delta\theta$ for KAM calculation is expressed by [42]:

9

10   $$\Delta\theta = \cos^{-1}\left(\frac{g_{11}+g_{22}+g_{33}-1}{2}\right). \qquad (2)$$

11

12   Fig. 2c shows a schematic of the calculation method for $\Delta\phi$. The crystal orientations of

13   the elements (i,j) and (k,l) are expressed as $\left(\phi_1^{ij},\Phi^{ij},\phi_2^{ij}\right)$ and $\left(\phi_1^{kl},\Phi^{kl},\phi_2^{kl}\right)$,

14   respectively. $\Phi^{ij}=\Phi^{kl}=0$ is temporarily assigned, and the minimum difference of angles

15   in $<11\bar{2}0>$ axes between the elements (i,j) and (k,l) is assumed to be $\Delta\phi$.

16   Activation of Pri<a> rotates the crystal orientations around the <0001> axis. We set

17   $\Phi^{ij}=\Phi^{kl}=0$ such that only the activity of the slip systems that causes this rotation

18   around the <0001> axis can be evaluated by $\Delta\phi$. Finally, a schematic of the calculation

19   method for $\Delta\Phi$ is shown in Fig. 2d. When the crystal orientations in elements (i,j)

20   and (k,l) are $\left(\phi_1^{ij},\Phi^{ij},\phi_2^{ij}\right)$ and $\left(\phi_1^{kl},\Phi^{kl},\phi_2^{kl}\right)$, the difference in the inclination angles

1   in the [0001] axes between (i,j) and (k,l) are calculated by $\Delta\Phi = \left|\Phi^{ij} - \Phi^{kl}\right|$.

2

3   **3. Experimental results**

4   **3.1 EBSD orientation maps, pole figures, and distributions of Schmid factors**

5   The changes in the EBSD orientation maps and (0001) pole figures under the uniaxial

6   tensile test are shown in Fig. 3. The nominal strains in the figures were calculated from

7   the changes in the length between specific grains during deformation. Nonuniformity in

8   crystal orientation distributions develops with the progress of deformation, and twinning

9   occurs. Fig. 4 shows the spatial distributions of the Schmid factors at a nominal strain of

10   0.0% in the tensile direction ($\varepsilon_n = 0.0\%$). The Schmid factors for Pri<a> are lower than

11   those for other slip systems. For the twin systems, the Schmid factors for the $\{10\bar{1}2\}$

12   tension twins in the tensile (X) direction are low, whereas the values for the $\{11\bar{2}2\}$

13   compression twins in the transverse direction (TD) (Y direction) are high.

14

15   **3.2 Active slip and twin systems**

16   Active deformation modes were identified. First, the active slip systems were estimated.

17   Fig. 5 shows the changes in distributions in KAM, KAM_a, and KAM_c, and the

18   intergranular misorientation axis (IGMA) [43][44][45] with the deformation. IGMA

14

1   indicates the axis of the slip-induced lattice rotation, as determined from the

2   crystallographic orientation difference in each grain. Thus, the active slip system can be

3   identified from the IGMA. Local misorientations develop in all regions, as indicated by

4   the KAM distributions (Fig. 5a). When the misorientations calculated from the individual

5   rotational axes are compared between KAM_a and KAM_c, the development of

6   misorientation around the [0001] axes (Fig. 5b KAM_a) is greater than that of the

7   inclination angle of the [0001] axes (Fig. 5c KAM_c). Misorientations around the [0001]

8   axes were induced by the activation of Pri<a>. Thus, Pri<a> was dominantly activated in

9   all regions, while the Schmid factors for this system were lower than those for other <a>

10   slip systems (Fig. 4a). The same tendency was observed from the IMGA distribution (Fig.

11   6d); the dominant rotational axis (Taylor axis) during deformation is [0001]. However,

12   regions with a high KAM_c were detected near the grain boundaries (Fig. 5c). The changes

13   in KAM_c are caused by the inclination of the [0001] axes; non-Pri<a> systems were

14   activated near the grain boundaries.

15

16   Next, an active twin system was identified. Table 2 shows the crystal orientations of the

17   matrix and twin regions at $\varepsilon_n = 8.4\%$ (Fig. 3a) and the rotational relationships of the

18   [0001] axes between these regions. The position numbers in Table 2 correspond to those

1   shown in Fig. 3a ($\varepsilon_n = 8.4\%$). The rotational relationships between the matrix and the

2   twin regions range from 64° to 66°, except for 33.1° at positions 10 and 11. Table 3 shows

3   the rotation angles of the [0001] axes induced by twinning. Typically, twin systems that

4   exhibit high activities at room temperature are the $\{10\bar{1}2\}$ tensile and $\{11\bar{2}2\}$

5   compression systems [3][34][46][47][48][49][50]. Tables 2 and 3 indicate that the

6    $\{11\bar{2}2\}$ compression twin system, rather than the $\{10\bar{1}2\}$ tensile system, dominates the

7   CP-Ti specimen. In split textures, where the aggregates of the [0001] axes are inclined

8   and split in TD or RD, $\{11\bar{2}2\}$ compression twinning is observed under uniaxial tensile

9   tests. Becker and Pantleon (2013) and Roth et al. (2014) observed that $\{11\bar{2}2\}$ twinning

10   was dominant when CP-Ti with a TD-split texture was pulled in the RD [29][30]. On the

11   other hand, Zheng et al. (2009) conducted compression tests of CP-Ti with RD-split

12   texture, in which the sample specimen was compressed in TD at 673–973 K, and the

13    $\{11\bar{2}2\}$ compression twin was not observed, and the active twin systems were $\{10\bar{1}2\}$

14   tension and $\{10\bar{1}1\}$ compression twins [31]. In other words, it is possible that the

15   compression and tension twin systems are dominantly activated under tensile and

16   compressive deformation, respectively. In this study, the tensile direction corresponded

17   to the splitting direction, and the dominant twin system was $\{11\bar{2}2\}$. The Schmid factors

18   for the $\{10\bar{1}2\}$ twins are low (Fig. 4a) under the current condition, and this prevents

1 $\{10\bar{1}2\}$ twinning under tensile loading. The causes of the $\{11\bar{2}2\}$ twinning observed

2 in this study are discussed in Section 5.

3

4 **4. Analysis by CPFE method and SOF**

5 CPFE and SOF analyses were conducted to investigate the activation conditions for the

6 slip and twin systems in more detail. The outline of the methods and conditions for these

7 analyses are described below.

8

9 **4.1 Numerical models for crystal plasticity analysis**

10 A rate-dependent finite-element crystal plasticity model [51][52] was employed. The

11 shear slip rate $\dot{\gamma}$ for slip system k is calculated as follows:

12

13 $$\dot{\gamma}^{(k)} = \dot{\gamma}_0 \, \mathrm{sgn}\left(\tau^{(k)}\right) \left|\frac{\tau^{(k)}}{\hat{\tau}^{(k)}}\right|^{\frac{1}{m}},\qquad\qquad (3)$$

14

15 where $\dot{\gamma}_0$, τ, $\hat{\tau}$, $\hat{\tau}$, and m are the reference shear strain rates for the plastic slip, RSS,

16 reference shear stress, and slip rate sensitivity parameter, respectively. $\hat{\tau}$ is provided by

17 the Voce hardening law [44][45], considering the interactions between slip systems as

18 follows:

19

1 $$\dot{g}^{(k)} = \frac{d\hat{\tau}^{(k)}}{d\Gamma} \sum_{l} h_{kl} \left| \dot{\gamma}^{(k)} \right|, \qquad\qquad (4)$$

2

3 $$\hat{\tau}^{(k)} = \tau_0^{(k)} + \left(\tau_1^{(k)} + \theta_1^{(k)} \Gamma \right) \left\{ 1 - \exp\left(-\frac{\theta_0^{(k)} \Gamma}{\tau_1^{(\alpha)}} \right) \right\}, \qquad (5)$$

4

5 where Γ is the cumulative shear strain, h_{kl} is the hardening matrix, and τ_0, τ_1, θ_0,

6 and θ_1 are the parameters that represent the relationship between the shear stress and

7 shear strain.

8

9 **4.2 Conditions for crystal plasticity analysis**

10 Fig. 6 shows the geometric models and boundary conditions employed for CPFE analysis.

11 Double and single-layer models were built as the geometric models. The crystal

12 orientation distributions in both models correspond to those in the EBSD orientation map

13 employed in the current CP-Ti specimen, and the EBSD orientation map (Fig. 1) was

14 converted into geometric models for CPFE analysis using the EBSD-FEM data

15 conversion procedure developed by Kawano et al. (2018) [55]. However, the double-layer

16 model consists of layers with crystal orientations reflecting the EBSD orientation map as

17 well as a layer with random crystal orientations to represent the effect of grains existing

18 in the depth (Z) direction on the inhomogeneous deformation. Crystal orientations in the

1   single-layer model were obtained only from the EBSD orientation map and were uniform

2   in the Z-direction. Zhang et al. (2018) also conducted CPFE analysis using a double-layer

3   and single-layer model and showed that the results obtained by the analyses were different

4   between the two models [25].

5

6   Tables 4 and 5 present the physical values employed in the CPFE analysis. The elastic

7   constants of pure Ti were used in the analysis. The parameters used for the Voce hardening

8   law are shown in Table 5, and $\hat{\tau}$ as a function of Γ, which determines the work

9   hardening properties and CRSS, are shown in Fig. 7. While CRSS for Pri<a> is typically

10   the lowest in all slip systems in CP-Ti, magnitude correlation of CRSSs between other

11   slip systems are unclear. The order of CRSSs among slip systems is different in previous

12   reports [6][16][7][56][57][58], making it still an open discussion [6]. In this study, the

13   initial CRSSs were determined based on Hama et al. (2017) [6] and the current

14   experimental results. The current CRSSs for Bsl<a>, Pri<a>, Pyr1<c+a>, and Pyr2<c+a>

15   are the same as those employed in Hama et al. (2017) [6], and those for Pyr1<a> were set

16   to be higher than those in Hama et al. (2017). The $\{10\bar{1}2\}$ and $\{11\bar{2}2\}$ twin systems

17   are assumed to be nonactive because the criterion for $\{11\bar{2}2\}$ twinning was investigated

18   without changing the stress field by the activation of twinning, and $\{10\bar{1}2\}$ twinning

19

1   was not observed in the experiment in this study.

2

4.3 Slip operation factor

4.3.1   Numerical model of SOF [38][39]

5   The SOF is an indicator that considers nonlocal interactions to evaluate the ease of

6   activation of the individual deformation modes. It is calculated with the relative ease of

7   plastic deformation between regions, considering the weight by distance between them,

8   as shown in Fig. 8 [38][39]. The SOF for deformation mode k is evaluated as follows:

9

10    $$\hat{M}_i^{\prime(k)} = M_i^{\prime(k)} + A^{LD}\hat{M}_i^{\prime LD,(k)} + A^{TD}\hat{M}_i^{\prime TD,(k)}, \qquad (6)$$

11

12   where i is the number of elements. M', $\hat{M}^{\prime LD}$, and $\hat{M}^{\prime TD}$, whose maximum value is

13   1.0, are the normalized values of M, $\hat{M}^{LD}$, and $\hat{M}^{TD}$, respectively. M, $\hat{M}^{LD}$, and

14    $\hat{M}^{TD}$ express the ease of plastic deformation considering multiple slips; M is the value

15   without considering mechanical interactions between regions; $\hat{M}^{LD}$ and $\hat{M}^{TD}$ are the

16   relative ease of plastic deformation considering the mechanical interactions in the loading

17   direction (LD) and the transverse direction (TD) to the LD, respectively. A^{LD} and A^{TD}

18   determine the magnitude of the mechanical interactions between the grains in the LD and

19   TD. M, $\hat{M}^{LD}$, and $\hat{M}^{TD}$ are described as follows.

20

21    $$M_i = \sum_k \left(A_i^{ord,(k)} \cdot m_i^{(k)} \cdot \frac{\tau_i^{\min}}{\tau_i^{(k)}} \right), \qquad (7)$$

1

$$\hat{M}_i^{LD,(k)} = \sum_{j \neq i} \left[w\left(\|\boldsymbol{r}_{ij}\|, r_e^{LD} \right) \cdot \min\left(\frac{M_i^{(k)}}{M_j}, R_{\max}^{LD} \right) \cdot \left| \cos \theta_{ij} \right| \right], \qquad (8)$$

3

$$\hat{M}_i^{TD,(k)} = \sum_{j \neq i} \left[w\left(\|\boldsymbol{r}_{ij}\|, r_e^{TD} \right) \cdot \min\left(\frac{M_j}{M_i^{(k)}}, R_{\max}^{TD} \right) \cdot \left| \sin \theta_{ij} \right| \right], \qquad (9)$$

5

6 where $m_i^{(k)}$ and $\tau_i^{(k)}$ are the Schmid factor and CRSS for deformation mode k,

7 respectively, and $\tau_i^{\min}$ is the minimum CRSS in all deformation modes in region i.

8 $m_i^{(k)} \cdot \tau_i^{\min} / \tau_i^{(k)}$ Equation (7) is the normalized Schmid factor (NSF) [59], which

9 represents the plastic deformability in region i considering the Schmid factor and CRSS.

10 $A_i^{ord,(k)}$ is the weight coefficient according to the ranking of the NSF of deformation

11 mode k in all deformation modes in region i. The deformation modes with higher $A_i^{ord,(k)}$

12 are activated more easily. w represents the effect of the interaction strength depending

13 on the distance $\|\boldsymbol{r}_{ij}\|$ between regions i and j, and r_e^{LD} and r_e^{TD} are the limits of the

14 interaction ranges in LD and TD, respectively. $R_{\max}^{LD}$ and $R_{\max}^{TD}$ are the upper limits of

15 these relative values, and θ_{ij} corresponds to the angle that the LD forms with the

16 position vector $\boldsymbol{r}_{ij}$ from region i to j (see Fig. 9). $\left| \cos \theta_{ij} \right|$ and $\left| \sin \theta_{ij} \right|$ provide the

17 components of the value in the directions parallel and perpendicular to the LD,

18 respectively.

1

2   w, in Eqs. (8) and (9), is expressed by the following weight function [39]:

3

4   $$w\left(r_{ij}, r_e\right) = \begin{cases} \left(1 - \dfrac{\|r_{ij}\|}{r_e}\right)^2, & 0 \le \|r_{ij}\| \le r_e \\ 0, & otherwise \end{cases} \quad (10)$$

5

6   where r_e is the interaction range. Equation (10) exhibits a bell curve, as shown in Fig.

7   8.

8

9   **4.3.2   Conditions for slip operation factor**

10 The SOF was calculated using the single-layer model employed in the CPFE analysis (Fig.

11 6c). The parameters used in the SOF analysis are presented in Table 6. It is assumed that

12 the three slip systems with the first, second, and third largest NSF are related to the

13 deformation, and in the weight coefficient A_i^{ord} in Eq. (7). The coefficients for the three

14 slip systems, A^{1st}, A^{2nd}, and A^{3rd}, were set to 1.0. For the other slip systems, A_i^{ord} was

15 assumed to be 0.0. Two conditions for A^{LD} and A^{TD} determining the magnitude of

16 mechanical interactions, and three conditions for r_e^{LD} and r_e^{RD} determining the

17 mechanical interaction range between regions, were used, as shown in Table 6.

1

2 **5. Numerical results and discussion**

3 **5.1 Reproduction of KAM distributions by CPFE analysis**

4 The KAM distributions obtained through CPFE analysis are shown in Figs. 9 and 10.

5 While KAM develops near the grain boundaries in both the double- and single-layer

6 models, regions with high KAM values exist inside the grains in the double-layer model.

7 Such regions in the double-layer model (Fig. 9) were larger than those in the single-layer

8 model (Fig. 10). This implies that the nonuniformity of deformation in the double-layer

9 model is more prominent than that in the single-layer model. Thus, a sublayer with a

10 random crystal orientation contributes to nonuniform deformation. This tendency

11 coincides with the results of Zhan et al. (2018) [25]. The distributions of KAM, KAM_a,

12 and KAM_c in the double-layer model (Fig. 9) agree with the experimental results (Fig. 5).

13

14 The frequency distributions of KAM, KAM_a, and KAM_c calculated from the results

15 obtained from the experiments and numerical simulations are shown in Fig. 11. The

16 frequency distributions show a wide range of distributions owing to the deformation,

17 indicating the development of nonuniform deformation. Additionally, since the activity

18 of Pri<a> is higher than those of non-Pri <a>, the distribution of KAM_a is wider than that

1   of KAMc. These frequency distributions obtained by numerical simulations, especially

2   in the double-layer model, agree with those obtained experimentally. These comparisons

3   quantitatively show that the experimental and numerical results were mutually consistent.

4   The development of local misorientation is derived from the activation of slip systems.

5   Therefore, these indicate that the current CPFE analysis using the double-layer model

6   accurately predicted the activity of the slip systems in the tensile test.

7

8   **5.2 Predicted strain distributions by CPFE analysis and SOF analysis**

9   Figs. 11a and b show the distributions of the normal slip strain in the tensile direction

10   (ε_{XX}) in the double-layer and single-layer models, respectively. The strain inside the

11   grains in the double-layer model tends to be higher than that in the single-layer model;

12   however, the strain distributions in both models were similar.

13

14   The strain distributions predicted by the CPFE analysis (Figs. 12a and b) were compared

15   with the SOF distributions in the tensile (X) direction (Fig. 12c). The distributions of the

16   SOF changed with the mechanical interaction range r_e^{LD} r_e^{TD}. When the interaction

17   range in the tensile direction is larger than or equal to that in the transverse direction

18   ($r_e^{LD} = 2D_{ave}$ $r_e^{TD} = D_{ave}$ or $r_e^{LD} = 2D_{ave}$ $r_e^{TD} = 2D_{ave}$), the SOF distributions

1 correspond well with the ε_{XX} distributions at $\varepsilon_n = 2.0\%$. However, the similarity

2 between the distributions decreased as deformation progressed. A similar relationship

3 among the prediction accuracy, employed parameters, and progress in the deformation

4 was obtained by Kawano et al. (2020) [38].

5

6 **5.3 Estimated position of** $\{11\bar{2}2\}$ **twin by SOF analysis**

7 The positions of $\{11\bar{2}2\}$ twins obtained experimentally were compared with those

8 estimated through the SOF analysis. Fig. 13 displays only the comparable areas among

9 the figures, and the twinning positions are indicated by arrows in Figs. 13a and b. The

10 SOF distributions are for the transverse (Y) direction rather than the loading (X) direction,

11 and LD and TD in r_e^{LD} and r_e^{TD} correspond to the Y and X directions, respectively.

12 When $r_e^{LD} = D_{ave}$ $r_e^{TD} = 2D_{ave}$ is employed, regions with high SOF values, indicated by

13 white arrows in Fig. 13b, coincide with the twinning positions. In contrast, the SOF

14 analysis failed to predict the twinning positions indicated by the black arrows in Fig. 13b.

15 The prediction accuracy of twinning was quite low under these conditions. The SOF

16 distribution obtained under the condition $r_e^{LD} = 2D_{ave}$ $r_e^{TD} = 2D_{ave}$ is intermediate

17 between those obtained through $r_e^{LD} = D_{ave}$ $r_e^{TD} = 2D_{ave}$ and $r_e^{LD} = 2D_{ave}$ $r_e^{TD} = D_{ave}$.

18 Thus, in the SOF analysis, the prediction accuracy for twinning is higher when the

1   interaction range in the transverse (Y) direction is longer than that in the tensile (X)

2   direction.

3

4   Regions with a high Schmid factor for $\{11\overline{2}2\}$ twins in the Y direction cover a large area

5   within the specimen, making it difficult to select the twinning positions in these regions.

6   The Schmid factor does not consider the effect of the mechanical interaction between

7   regions, which is considered in the SOF. Due to the higher prediction accuracy of the

8    $\{11\overline{2}2\}$ twinning positions in the SOF analysis than in the Schmid factor calculations,

9   this mechanical interaction plays an important role in the $\{11\overline{2}2\}$ twinning. Fig. 14

10   shows the SOF distributions for the $\{11\overline{2}2\}$ twin system obtained under the condition

11   that the magnitude of the interactions A^{LD}, A^{TD} is five times higher than those in Fig.

12   13. The distributions in Fig. 14 are similar to those in Fig. 13, which means that the

13   magnitudes of the mechanical interactions between regions play an important role, i.e.,

14   mechanical interaction terms (the second and third terms on the right side of Eq. (6))

15   govern the SOF distributions under both conditions: A^{LD} and A^{TD}. It has been pointed

16   out that deformation incompatibility strongly affects twin nucleation and growth [14][36],

17   and this tendency corresponds to the results obtained through the SOF analysis.

18

26

5.4   Criteria of $\{11\bar{2}2\}$ twin activation estimated by experiment, SOF, and CPFE

analysis

Fig. 15 shows the stress distributions in the double-layer model at the elastic ($\varepsilon_n = 0.1\%$)

and plastic ranges ($\varepsilon_n = 8.4\%$) using the CPFE analysis. Nonuniformity in the

distributions of the normal stress in the tensile direction (σ_{XX}) developed with plastic

deformation (Figs. 15a and d), and compressive stresses occurred locally even though

tensile loading was applied (Fig. 15d). However, the positions with high compressive

stresses differ from those of the $\{11\bar{2}2\}$ twinning. Therefore, the compressive stresses

induced by inhomogeneous deformation is not a direct cause of $\{11\bar{2}2\}$ twinning. In

contrast, positions with high RSS for $\{11\bar{2}2\}$ twins (Figs. 14b and e) correspond well

with the twinning positions. The twinning positions that were successfully predicted are

indicated by white arrows; the others are indicated by black arrows. High RSS regions

tend to coincide with the twinning positions, and this tendency is stronger in the plastic

range than in the elastic range. The RSS concentration developed within the grains in the

plastic range, and the positions corresponded to the twinning positions. This implies that

the twinning positions within grains can be estimated by the RSS when plastic

deformation is considered. Therefore, the development of an RSS with inhomogeneous

deformation is more important for $\{11\bar{2}2\}$ twinning in the current CP-Ti specimen than

1   the compressive stresses.

2

3   However, the RSS distribution did not completely predict the twinning positions. The

4   same tendency, where a high RSS region has good correspondence with twinning

5   positions but is not complete, was observed in the elastic deformation analysis of CP-Ti

6   conducted by Lind et al. (2014) [36]. The current CPFE analysis considered not only the

7   elastic deformation but also the stress redistribution with plastic deformation, and the

8   results indicate that criterion(s) other than RSS for $\{11\bar{2}2\}$ twinning exist(s). Lind et al.

9   (2014)[36] studied the effect of the Schmid factor, RSS, and single neighbor slip

10   compatibility on twinning, and found that these factors are invalid for the low Schmid

11   factor case for twins. Bieler et al. (2014) [32] indicated that slip transfer across grain

12   boundaries is an important factor for twinning. Zhou et al. (2021) reported that twinning

13   in regions with a low Schmid factor could be predicted by the displacement gradient

14   tensor and geometric compatibility factor, which evaluate the strain accommodation

15   between grains [50]. $\{11\bar{2}2\}$ twinning in the current study is typically observed in

16   regions with a high Schmid factor. Thus, we discuss the criterion of $\{11\bar{2}2\}$ twinning in

17   this case.

18

1   In hcp materials, atomic shuffling is required to achieve the right twin-orientation

2   relationship [15][60]. Atomic shuffling and twin nucleation are affected by the

3   interatomic distance, which is also closely related to the relationship between twinning

4   and hydrostatic pressure. Figs. 15c and f show the distributions of hydrostatic pressure

5   (σ_{hp}). The arrows indicate the twinning positions, where the white arrows correspond to

6   the high σ_{hp} regions. Twinning typically occurred in high σ_{hp} regions, especially in

7   the plastic range (Fig. 15f). However, twinning was not predicted in the two regions,

8   which are indicated by black arrows in the σ_{hp} distribution even in the plastic range

9   (Fig. 15f). The twinning position (Fig. 15f) was successfully predicted using the RSS

10   criterion previously for one of these two regions (Fig. 15e). In contrast, the positions

11   indicated by the other black arrow enclosed with circle fail to be predicted by both $\tau_{11\bar{2}\bar{2}}$

12   and σ_{hp} , implying that other criterion(s) for twinning exist(s).

13

14   The above results indicate that SOF is an efficient tool for the prediction of twinning, and

15   that hydrostatic pressure and RSS are related to the criteria used in a continuum body.

16   Furthermore, it is possible that slip transfer between grains [61], dislocation density [28],

17   and other factors increase the prediction accuracy for twinning. The evaluation of these

18   effects on twinning will be addressed in the future.

19

6. Conclusion

CP-Ti with RD-split texture was pulled in the RD, and the development of crystal

orientation distribution under deformation was observed by EBSD. Local misorientation

was evaluated using KAM. CPFE analysis was conducted, and the development of the

KAM distributions was reproduced. SOF analysis was also performed to predict the

positions of $\{11\bar{2}2\}$ compression twinning. The criteria for twinning are discussed

based on the results obtained from the experiments and numerical analyses. The results

are summarized as follows:

1. KAM distributions and experimentally obtained IGMA showed that Pri<a> was

   dominantly activated in the whole region, while the non-Pri<a> was activated

   typically near the grain boundary.

2. $\{10\bar{1}2\}$ Tensile twins were not observed during tensile deformation. Instead, the

   $\{11\bar{2}2\}$ compression twin was predominantly activated. It is inferred that the low

   Schmid factor and high RSS for the $\{10\bar{1}2\}$ and $\{11\bar{2}2\}$ twins, respectively,

   significantly affected the activation of twin systems.

3. The RSS predicts the $\{11\bar{2}2\}$ twinning positions more accurately when plastic

   deformation is considered. However, the prediction was not complete when the RSS

1   criterion was solely used, and other criteria exist for $\{11\overline{2}2\}$ twinning. In this case,

2   hydrostatic pressure may be one of the criteria for a continuum body.

3   4. The SOF predicts the twinning positions with the same degree of accuracy as the

4   CPFE analysis using the RSS criterion when the direction (Y direction) perpendicular

5   to the actual loading direction (X direction) was employed as the loading direction in

6   SOF calculation. In this calculation, the mechanical interaction range for twinning

7   was longer in the X direction than that in the Y direction. Furthermore, the twin

8   activation was more strongly influenced by the difference in twinning resistance

9   between neighboring grains than by the twinning resistance itself in each grain which

10   was calculated from SF and CRSS for twinning.

11

18

31

1 **References**

2 [1] G. Lütjering, J.C. Williams, Titanium, 2nd Edition (Engineering and Processes),

3   Springer Berlin Heidelberg, Berlin, Heidelberg, 2007.

4   https://doi.org/10.1007/978-3-540-73036-1.

5 [2] S. Nemat-Nasser, W.G. Guo, J.Y. Cheng, Mechanical properties and deformation

6   mechanisms of a commercially pure titanium, Acta Mater. 47 (1999) 3705–3720.

7   https://doi.org/10.1016/S1359-6454(99)00203-7.

8 [3] Y.B. Chun, S.H. Yu, S.L. Semiatin, S.K. Hwang, Effect of deformation twinning

9   on microstructure and texture evolution during cold rolling of CP-titanium,

10   Mater. Sci. Eng. A. 398 (2005) 209–219.

11   https://doi.org/10.1016/j.msea.2005.03.019.

12 [4] A.A. Salem, S.R. Kalidindi, R.D. Doherty, Strain hardening of titanium: Role of

13   deformation twinning, Acta Mater. 51 (2003) 4225–4237.

14   https://doi.org/10.1016/S1359-6454(03)00239-8.

15 [5] A.A. Salem, S.R. Kalidindi, S.L. Semiatin, Strain hardening due to deformation

16   twinning in α-titanium: Constitutive relations and crystal-plasticity modeling,

17   Acta Mater. 53 (2005) 3495–3502.

18   https://doi.org/10.1016/j.actamat.2005.04.014.

1   [6]   T. Hama, A. Kobuki, H. Takuda, Crystal-plasticity finite-element analysis of

2   anisotropic deformation behavior in a commercially pure titanium Grade 1 sheet,

3   Int. J. Plast. 91 (2017) 77–108. https://doi.org/10.1016/j.ijplas.2016.12.005.

4   [7]   J.L.W. Warwick, N.G. Jones, K.M. Rahman, D. Dye, Lattice strain evolution

5   during tensile and compressive loading of CP Ti, Acta Mater. 60 (2012) 6720–

6   6731. https://doi.org/10.1016/j.actamat.2012.08.042.

7   [8]   M.S. Lee, A.R. Jo, S.K. Hwang, Y.T. Hyun, T.S. Jun, The role of strain rate and

8   texture in the deformation of commercially pure titanium at cryogenic

9   temperature, Mater. Sci. Eng. A. 827 (2021).

10   https://doi.org/10.1016/j.msea.2021.142042.

11 [9]   J. Li, P. Zhang, L. Lu, F. Lv, X.T. Miao, L. Chang, B. Bin Zhou, X.H. He, C.Y.

12   Zhou, Effect of pre-strain on fatigue crack growth behavior for commercial pure

13   titanium at ambient temperature, Int. J. Fatigue. 117 (2018) 27–38.

14   https://doi.org/10.1016/j.ijfatigue.2018.07.036.

15 [10] L. Chang, B. Bin Zhou, T.H. Ma, J. Li, X.H. He, C.Y. Zhou, The difference in

16   low cycle fatigue behavior of CP-Ti under fully reversed strain and stress

17   controlled modes along rolling direction, Mater. Sci. Eng. A. 742 (2019) 211–

18   223. https://doi.org/10.1016/j.msea.2018.11.003.

1   [11]   N. Bosh, C. Müller, H. Mozaffari-Jovein, Deformation twinning in cp-Ti and its

2   effect on fatigue cracking, Mater. Charact. 155 (2019).

3   https://doi.org/10.1016/j.matchar.2019.109810.

4   [12]   G. Kim, S.A.A. Shams, J.N. Kim, J.W. Won, S.W. Choi, J.K. Hong, C.S. Lee,

5   Enhancing low-cycle fatigue life of commercially-pure Ti by deformation at

6   cryogenic temperature, Mater. Sci. Eng. A. 803 (2021) 140698.

7   https://doi.org/10.1016/j.msea.2020.140698.

8   [13]   S.J. Lainé, K.M. Knowles, Deformation twinning in commercial purity titanium

9   at room temperature, Philos. Mag. 95 (2015) 2153–2166.

10   https://doi.org/10.1080/14786435.2015.1051157.

11   [14]   Y. Guo, H. Abdolvand, T.B. Britton, A.J. Wilkinson, Growth of $\{11\bar{2}2\}$ twins

12   in titanium: A combined experimental and modelling investigation of the local

13   state of deformation, Acta Mater. 126 (2017) 221–235.

14   https://doi.org/10.1016/j.actamat.2016.12.066.

15   [15]   G. Tsukamoto, T. Kunieda, S. Yamasaki, M. Mitsuhara, H. Nakashima, Effects

16   of temperature and grain size on active twinning systems in commercially pure

17   titanium, J. Alloys Compd. 884 (2021) 161154.

18   https://doi.org/10.1016/j.jallcom.2021.161154.

1   [16]   H. Conrad, Effect of interstitial solutes on the strength and ductility of titanium,

2   Prog. Mater. Sci. 26 (1981) 123–403. https://doi.org/10.1016/0079-

3   6425(81)90001-3.

4   [17]   Y. Kawano, T. Ohashi, T. Mayama, M. Tanaka, Y. Okuyama, M. Sato,

5   Investigation of strain redistribution mechanism in α titanium by image-based

6   crystal plasticity analysis, Eur. Phys. J. B. 92 (2019) 204.

7   https://doi.org/10.1140/epjb/e2019-100238-3.

8   [18]   Y. Xiong, P. Karamched, C.T. Nguyen, D.M. Collins, C.M. Magazzeni, E.

9   Tarleton, A.J. Wilkinson, Cold creep of titanium: Analysis of stress relaxation

10   using synchrotron diffraction and crystal plasticity simulations, Acta Mater. 199

11   (2020) 561–577. https://doi.org/10.1016/j.actamat.2020.08.010.

12   [19]   A. Guery, F. Hild, F. Latourte, S. Roux, Slip activities in polycrystals determined

13   by coupling DIC measurements with crystal plasticity calculations, Int. J. Plast.

14   81 (2016) 249–266. https://doi.org/10.1016/j.ijplas.2016.01.008.

15   [20]   P. Baudoin, T. Hama, H. Takuda, Influence of critical resolved shear stress ratios

16   on the response of a commercially pure titanium oligocrystal: Crystal plasticity

17   simulations and experiment, Int. J. Plast. 115 (2019) 111–131.

18   https://doi.org/10.1016/j.ijplas.2018.11.013.

1   [21] P. Baudoin, T. Hama, S. Uchida, H. Takuda, Crystal plasticity analysis of the

2   deformation of a grade 2 CP-Ti oligocrystal, J. Phys. Conf. Ser. 1063 (2018)

3   012048. https://doi.org/10.1088/1742-6596/1063/1/012048.

4   [22] T. Mayama, T. Ohashi, R. Kondou, Geometrically necessary dislocation structure

5   organization in FCC bicrystal subjected to cyclic plasticity, Int. J. Plast. 25

6   (2009) 2122–2140. https://doi.org/10.1016/j.ijplas.2009.02.001.

7   [23] Y. Kawano, N. Tamaru, S. Ishii, T. Mayama, R. Kondou, T. Ohashi, Grain

8   boundary inclination dependence of GN dislocation patterns and density in

9   bicrystal model, Trans. JSME (in Japanese). 81 (2015) 14-00630-14–00630.

10   https://doi.org/10.1299/transjsme.14-00630.

11   [24] Y. Kawano, T. Ohashi, T. Mayama, R. Kondou, Crystal plasticity analysis of

12   change in incompatibility and activities of slip systems in α-phase of Ti alloy

13   under cyclic loading, Int. J. Mech. Sci. 146–147 (2018) 475–485.

14   https://doi.org/10.1016/j.ijmecsci.2017.09.023.

15   [25] Z. Zhang, D. Lunt, H. Abdolvand, A.J. Wilkinson, M. Preuss, F.P.E. Dunne,

16   Quantitative investigation of micro slip and localization in polycrystalline

17   materials under uniaxial tension, Int. J. Plast. 108 (2018) 88–106.

18   https://doi.org/10.1016/j.ijplas.2018.04.014.

1   [26] R.A. Lebensohn, C.N. Tomé, A study of the stress state associated with twin

2   nucleation and propagation in anisotropic materials, Philos. Mag. A. 67 (1993)

3   187–206. https://doi.org/10.1080/01418619308207151.

4   [27] J.J. Jonas, S. Mu, T. Al-Samman, G. Gottstein, L. Jiang, E. Martin, The role of

5   strain accommodation during the variant selection of primary twins in

6   magnesium, Acta Mater. 59 (2011) 2046–2056.

7   https://doi.org/10.1016/j.actamat.2010.12.005.

8   [28] Y. Guo, J. Schwiedrzik, J. Michler, X. Maeder, On the nucleation and growth of

9   {112-2} twin in commercial purity titanium: In situ investigation of the local

10   stress field and dislocation density distribution, Acta Mater. 120 (2016) 292–301.

11   https://doi.org/10.1016/j.actamat.2016.08.073.

12   [29] H. Becker, W. Pantleon, Work-hardening stages and deformation mechanism

13   maps during tensile deformation of commercially pure titanium, Comput. Mater.

14   Sci. 76 (2013) 52–59. https://doi.org/10.1016/j.commatsci.2013.03.028.

15   [30] A. Roth, M.A. Lebyodkin, T.A. Lebedkina, J.S. Lecomte, T. Richeton, K.E.K.

16   Amouzou, Mechanisms of anisotropy of mechanical properties of α-titanium in

17   tension conditions, Mater. Sci. Eng. A. 596 (2014) 236–243.

18   https://doi.org/10.1016/j.msea.2013.12.061.

1   [31]   Z. Zeng, S. Jonsson, H.J. Roven, The effects of deformation conditions on

2   microstructure and texture of commercially pure Ti, Acta Mater. 57 (2009) 5822–

3   5833. https://doi.org/10.1016/j.actamat.2009.08.016.

4   [32]   T.R. Bieler, L. Wang, A.J. Beaudoin, P. Kenesei, U. Lienert, In Situ

5   Characterization of Twin Nucleation in Pure Ti Using 3D-XRD, Metall. Mater.

6   Trans. A. 45 (2014) 109–122. https://doi.org/10.1007/s11661-013-2082-3.

7   [33]   H. Inoue, Textures in titanium and titanium alloys (in Japanese), Metal. 69

8   (1999) 30–38.

9   [34]   K.E.K. Amouzou, T. Richeton, A. Roth, M.A. Lebyodkin, T.A. Lebedkina,

10   Micromechanical modeling of hardening mechanisms in commercially pure α-

11   titanium in tensile condition, Int. J. Plast. 80 (2016) 222–240.

12   https://doi.org/10.1016/j.ijplas.2015.09.008.

13   [35]   C. Ma, H. Wang, T. Hama, X. Guo, X. Mao, J. Wang, P. Wu, Twinning and

14   detwinning behaviors of commercially pure titanium sheets, Int. J. Plast. 121

15   (2019) 261–279. https://doi.org/10.1016/j.ijplas.2019.06.010.

16   [36]   J. Lind, S.F. Li, R. Pokharel, U. Lienert, A.D. Rollett, R.M. Suter, Tensile twin

17   nucleation events coupled to neighboring slip observed in three dimensions, Acta

18   Mater. 76 (2014) 213–220. https://doi.org/10.1016/j.actamat.2014.04.050.

1   [37] Y. Yang, L. Wang, T.R. Bieler, P. Eisenlohr, M.A. Crimp, Quantitative atomic

2   force microscopy characterization and crystal plasticity finite element modeling

3   of heterogeneous deformation in commercial purity titanium, Metall. Mater.

4   Trans. A Phys. Metall. Mater. Sci. 42 (2011) 636–644.

5   https://doi.org/10.1007/s11661-010-0475-0.

6   [38] Y. Kawano, M. Sato, T. Mayama, M. Mitsuhara, S. Yamasaki, Quantitative

7   evaluation of slip activity in polycrystalline α-titanium considering non-local

8   interactions between crystal grains, Int. J. Plast. 127 (2020) 102638.

9   https://doi.org/10.1016/j.ijplas.2019.12.001.

10   [39] Y. Kawano, T. Mayama, M. Mitsuhara, S. Yamasaki, M. Sato, Generalized Slip

11   Operation Factor Considering Contribution of Secondary Slip Systems, Mater.

12   Today Commun. 26 (2021). https://doi.org/10.1016/j.mtcomm.2021.102041.

13   [40] C. Zhang, H. Li, P. Eisenlohr, W. Liu, C.J. Boehlert, M.A. Crimp, T.R. Bieler,

14   Effect of realistic 3D microstructure in crystal plasticity finite element analysis of

15   polycrystalline Ti-5Al-2.5Sn, Int. J. Plast. 69 (2015) 21–35.

16   https://doi.org/10.1016/j.ijplas.2015.01.003.

17   [41] H.J. Bunge, Texture Analysis in Materials Science, Elsevier, 1982.

18   https://doi.org/10.1016/C2013-0-11769-2.

1   [42] G. Zhu, W. Mao, Y. Yu, Calculation of Misorientation Distribution, Scr. Mater.

2   42 (2000) 37–41.

3   [43] Y.B. Chun, M. Battaini, C.H.J. Davies, S.K. Hwang, Distribution characteristics

4   of in-grain misorientation axes in cold-rolled commercially pure titanium and

5   their correlation with active slip modes, Metall. Mater. Trans. A Phys. Metall.

6   Mater. Sci. 41 (2010) 3473–3487. https://doi.org/10.1007/s11661-010-0410-4.

7   [44] Y.B. Chun, C.H.J. Davies, Investigation of prism $\langle a \rangle$ slip in warm-rolled

8   AZ31 alloy, Metall. Mater. Trans. A Phys. Metall. Mater. Sci. 42 (2011) 4113–

9   4125. https://doi.org/10.1007/s11661-011-0800-2.

10   [45] M. Yamasaki, K. Hagihara, S.I. Inoue, J.P. Hadorn, Y. Kawamura,

11   Crystallographic classification of kink bands in an extruded Mg-Zn-Y alloy using

12   intragranular misorientation axis analysis, Acta Mater. 61 (2013) 2065–2076.

13   https://doi.org/10.1016/j.actamat.2012.12.026.

14   [46] W. Tirry, S. Bouvier, N. Benmhenni, W. Hammami, A.M. Habraken, F. Coghe,

15   D. Schryvers, L. Rabet, Twinning in pure Ti subjected to monotonic simple shear

16   deformation, Mater. Charact. 72 (2012) 24–36.

17   https://doi.org/10.1016/j.matchar.2012.07.001.

18   [47] S. Xu, L.S. Toth, C. Schuman, J.-S. Lecomte, M.R. Barnett, Dislocation

mediated variant selection for secondary twinning in compression of pure

titanium, Acta Mater. 124 (2017) 59–70.

https://doi.org/10.1016/j.actamat.2016.10.063.

[48] K. Kishida, J.G. Kim, T. Nagae, H. Inui, Experimental evaluation of critical

resolved shear stress for the first-order pyramidal c + a slip in commercially pure

Ti by micropillar compression method, Acta Mater. 196 (2020) 168–174.

https://doi.org/10.1016/j.actamat.2020.06.043.

[49] S.W. Choi, J.S. Jeong, J.W. Won, J.K. Hong, Y.S. Choi, Grade-4 commercially

pure titanium with ultrahigh strength achieved by twinning-induced grain

refinement through cryogenic deformation, J. Mater. Sci. Technol. 66 (2021)

193–201. https://doi.org/10.1016/j.jmst.2020.04.082.

[50] B. Zhou, R. Yang, B. Wang, L. Deng, Y. Zhang, Twinning behavior of pure

titanium during rolling at room and cryogenic temperatures, Mater. Sci. Eng. A.

803 (2021) 140458. https://doi.org/10.1016/j.msea.2020.140458.

[51] D. Peirce, R.J. Asaro, A. Needleman, Material rate dependence and localized

deformation in crystalline solids, Acta Metall. (1983).

https://doi.org/10.1016/0001-6160(83)90014-7.

[52] R.J. Asaro, A. Needleman, Texture development and strain hardening in rate

1   dependent polycrystals, Acta Metall. 33 (1985) 923–953.

2   https://doi.org/10.1016/0001-6160(85)90188-9.

3 [53] E. Voce, A practical strain-hardening function, Metallurgia. 51 (1955) 219–226.

4 [54] U.F. Kocks, Laws for Work-Hardening and Low-Temperature Creep, J. Eng.

5   Mater. Technol. 98 (1976) 76–85. https://doi.org/10.1115/1.3443340.

6 [55] Y. Kawano, T. Ohashi, T. Mayama, M. Tanaka, M. Sakamoto, Y. Okuyama, M.

7   Sato, Development of a EBSD-FEM data conversion interface and the image-

8   based crystal plasticity analysis, Trans. JSME (in Japanese). 84 (2018) 17-

9   00559:1–18. https://doi.org/10.1299/transjsme.17-00559.

10 [56] M.J. Philippe, M. Serghat, P. Vanhoutte, C. Esling, Modeling of texture

11   evolution for materials of hexagonal symmetry -II. application to zirconium and

12   titanium α or near α alloys, Acta Metall. 43 (1995) 1619–1630.

13   https://doi.org/10.1016/0956-7151(94)00329-g.

14 [57] X. Wu, S.R. Kalidindi, C. Necker, A.A. Salem, Prediction of crystallographic

15   texture evolution and anisotropic stress-strain curves during large plastic strains

16   in high purity α-titanium using a Taylor-type crystal plasticity model, Acta

17   Mater. 55 (2007) 423–432. https://doi.org/10.1016/j.actamat.2006.08.034.

18 [58] N. Benmhenni, S. Bouvier, R. Brenner, T. Chauveau, B. Bacroix,

1   Micromechanical modelling of monotonic loading of CP α-Ti: Correlation

2   between macroscopic and microscopic behaviour, Mater. Sci. Eng. A. 573 (2013)

3   222–233. https://doi.org/10.1016/j.msea.2013.02.022.

4 [59] I. Bantounas, D. Dye, T.C. Lindley, The effect of grain orientation on fracture

5   morphology during high-cycle fatigue of Ti–6Al–4V, Acta Mater. 57 (2009)

6   3584–3595. https://doi.org/10.1016/j.actamat.2009.04.018.

7 [60] J.W. Christian, S. Mahajan, Deformation twinning, Prog. Mater. Sci. 39 (1995)

8   1–157. https://doi.org/10.1016/0079-6425(94)00007-7.

9 [61] T.R. Bieler, P. Eisenlohr, C. Zhang, H.J. Phukan, M.A. Crimp, Grain boundaries

10   and interfaces in slip transfer, Curr. Opin. Solid State Mater. Sci. 18 (2014) 212–

11   226. https://doi.org/10.1016/j.cossms.2014.05.003.

12 [62] Y. Zhong, F. Yin, K. Nagai, Role of deformation twin on texture evolution in

13   cold-rolled commercial-purity Ti, J. Mater. Res. 23 (2008) 2954–2966.

14   https://doi.org/10.1557/JMR.2008.0354.

15 [63] E.S. Fisher, C.J. Renken, Single-crystal elastic moduli and the hcp → bcc

16   transformation in Ti, Zr, and Hf, Phys. Rev. 135 (1964) A482–A494.

17   https://doi.org/10.1103/PhysRev.135.A482.

18

1   **Figure and table captions**

2

3   Fig. 1 Geometry of the CP-Ti specimen (a), the EBSD orientation map plotted for the ND

4   (b), and the (0001) pole figure (c).

5

6   Fig. 2 Schematic of the calculation method of the local misorientation angle. (a)

7   Relationship between address and elements when the microstructural map is divided into

8   rectangular solid elements. (b) Crystal lattice coordinate system when the Euler angles

9    $(\phi_1, \Phi, \phi_2) = (0,0,0)$. Calculation method of misorientation angle around [0001] axis (c)

10   and of [0001] axes (d) between positions (i, j) and (k, l).

11

12   Fig. 3 Changes in EBSD orientation map plotted for the ND (a) and (0001) pole figures

13   (b) under uniaxial tension.

14

15

16   Fig. 4 Distributions of Schmid factors of slip systems (a), and twin systems (b).

17

18   Fig. 5 Development of KAM distributions (a-c) and in-grain misorientation axis (IGMA)

1   (d) under uniaxial tensile deformation. KAM calculated from the difference of angles $\Delta\theta$

2   (Eq. 2) (a), misorientation angles $\Delta\phi$ around [0001] axis (b), and difference of inclination

3   angles $\Delta\Phi$ of [0001] axes (c). IGMA with misorientation angles $\leqq$ 2° are plotted in the

4   pole figures (d).

5

6   Fig. 6 Vertical cross-sectional views of the geometric models (a-c) and the boundary

7   conditions (d) for the uniaxial tensile analysis. The models were built based on Fig.

8   1a using EBSD-FEM data conversion procedure developed by Kawano et al. [46], and

9   the crystal orientations reflect the inverse pole figure while the crystal orientations in the

10   elements belonging to one layer contacting with the surface at Z = 0.0 μm are randomly

11   given in the double-layer model as shown in the figure (b). The surface at X = 0.0 is fixed

12   in X direction, the surface at Z = 0.0 is fixed in Z direction, and the forced displacement

13   is adapted to the right-hand surface (d). The strain rate is $1.0 \times 10^{-3}\,\mathrm{s^{-1}}$ for all deformation

14   simulations.

15

16   Fig. 7 CRSS for each deformation mode as a function of cumulative slip strain

17

18   Fig. 8 CRSS for each deformation mode as a function of cumulative slip strain [39]

1

2 Fig. 9 KAM distributions numerically reproduced using the double-layer model. KAM

3 calculated from the difference of angles $\Delta\theta$ (Eq. 2) (a), misorientation angles $\Delta\phi$ around

4 [0001] axis (b), and difference of inclination angles $\Delta\Phi$ of [0001] axes (c).

5

6 Fig. 10 KAM distributions numerically reproduced using the single-layer model. KAM

7 calculated from the difference of angles $\Delta\theta$ (Eq. 2) (a), misorientation angles $\Delta\phi$ around

8 [0001] axis (b), and difference of inclination angles $\Delta\Phi$ of [0001] axes (c).

9

10 Fig. 11 Frequency distributions of KAM, KAM_a, and KAM_c at $\varepsilon_n = 0.0\ \%$ (a-c) and 8.4 %

11 (d-f). The distributions at the initial state ($\varepsilon_n = 0.0\ \%$) are the same among those in the

12 experiment (Exp.), double-layer model, and single-layer model.

13

14 Fig. 12 Strain distributions obtained by CPFE analysis employing (a) double and (b)

15 single layer model. (c) SOF distributions for the X-directional tension. In the SOF

16 distributions, measuring $2D_{ave}$ from the outsides were strongly affected by boundary

17 conditions, and they removed from four sides of the models.

18

Fig. 13 Comparison of twinning positions. The inverse pole figure obtained by the experiment when the nominal strain is 8.4 % (a) and distributions of SOF for Y-direction for $\{11\bar{2}2\}$ twin (b-d). Arrows in the figures indicate twin positions. The white arrows in the figure (b) show the successfully predicted twin positions by SOF.

Fig. 14 SOF distributions for $\{11\bar{2}2\}$ twin when effect of mechanical interactions between regions are strong. Regions indicated by arrows are twinning positions observed in the experiment. The white arrows in the figures show the successfully predicted twin positions by SOF.

Fig. 15 Stress distributions obtained by CPFE analysis using the double-layer model. (a-c) elastic range and (d-f) plastic range. (a,d) normal stress in the tensile direction (σ_{XX}), (b,e) resolved shear stress for $\{11\bar{2}2\}$ twin ($\tau_{11\bar{2}\bar{2}}$), and (d) hydrostatic pressure (σ^{hp}). Color counters for $\tau_{11\bar{2}\bar{2}}$ and σ^{hp} are adjusted to observe high stress regions easily. Arrows in the figures indicate twin positions. Successfully predicted twin positions by higher stresses are indicated by white arrows in the figures.

Table 1 Chemical composition of the sample material [wt.%].

1

2 Table 2 Difference of <0001> axes between matrix and twin and estimated twin types.

3

4 Table 3 Twinning systems in α-Ti [62].

5

6 Table 4 Elastic compliance of pure titanium [(TPa)$^{-1}$] [63].

7

8 Table 5 Parameters for CPFE analysis and SOF calculation [MPa].

9

10 Table 6 Parameters employed in SOF calculation. D_{ave} (69.2 μm) is an average grain size
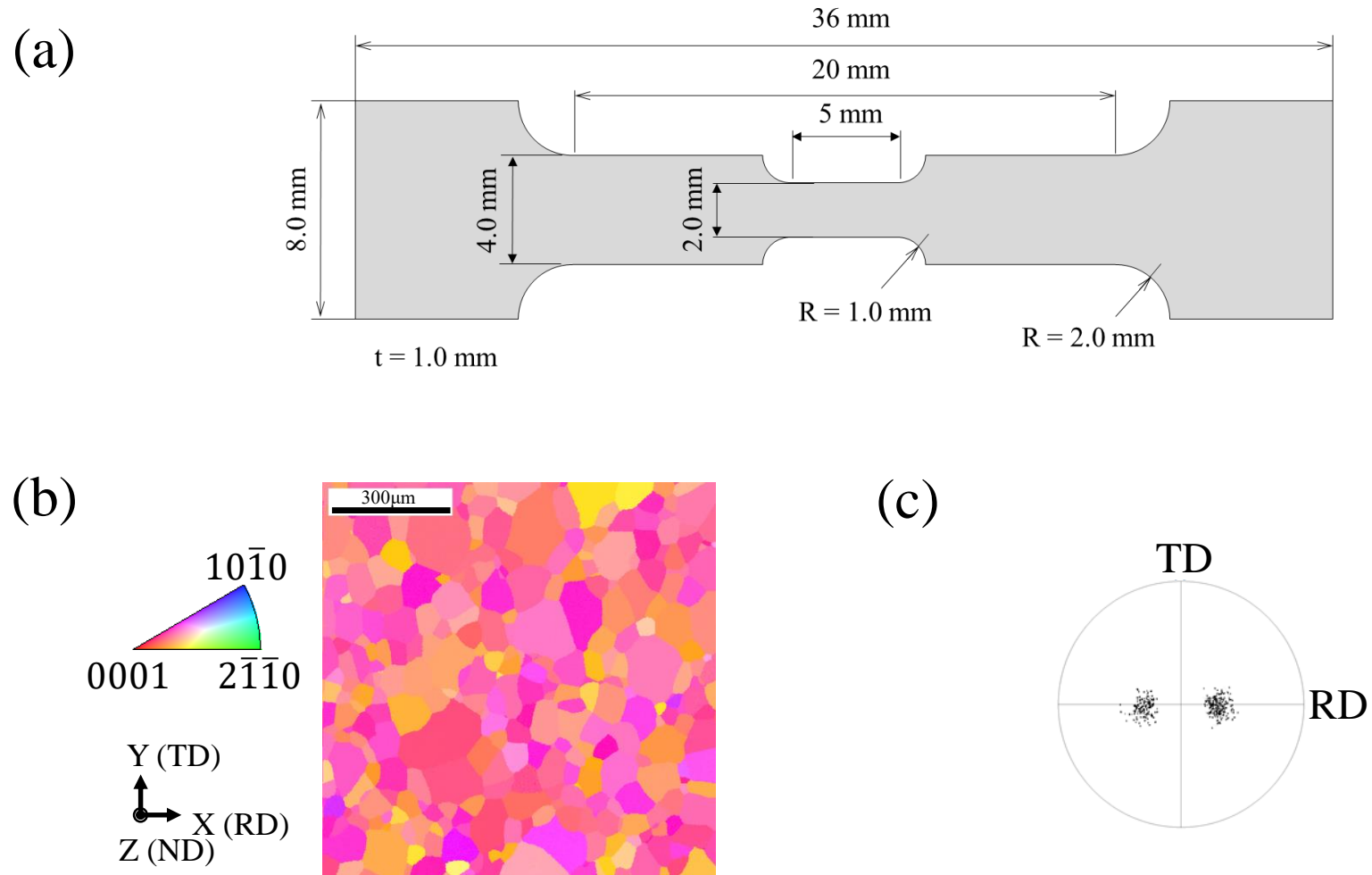
11 in the specimen.

Graphical abstract

$\varepsilon_n = 8.4\%$

$\widehat{m}'$

Slip operation factor

$\tau_{11\bar{2}2}$ [MPa]

σ_{hp} [MPa]

Crystal plasticity analysis
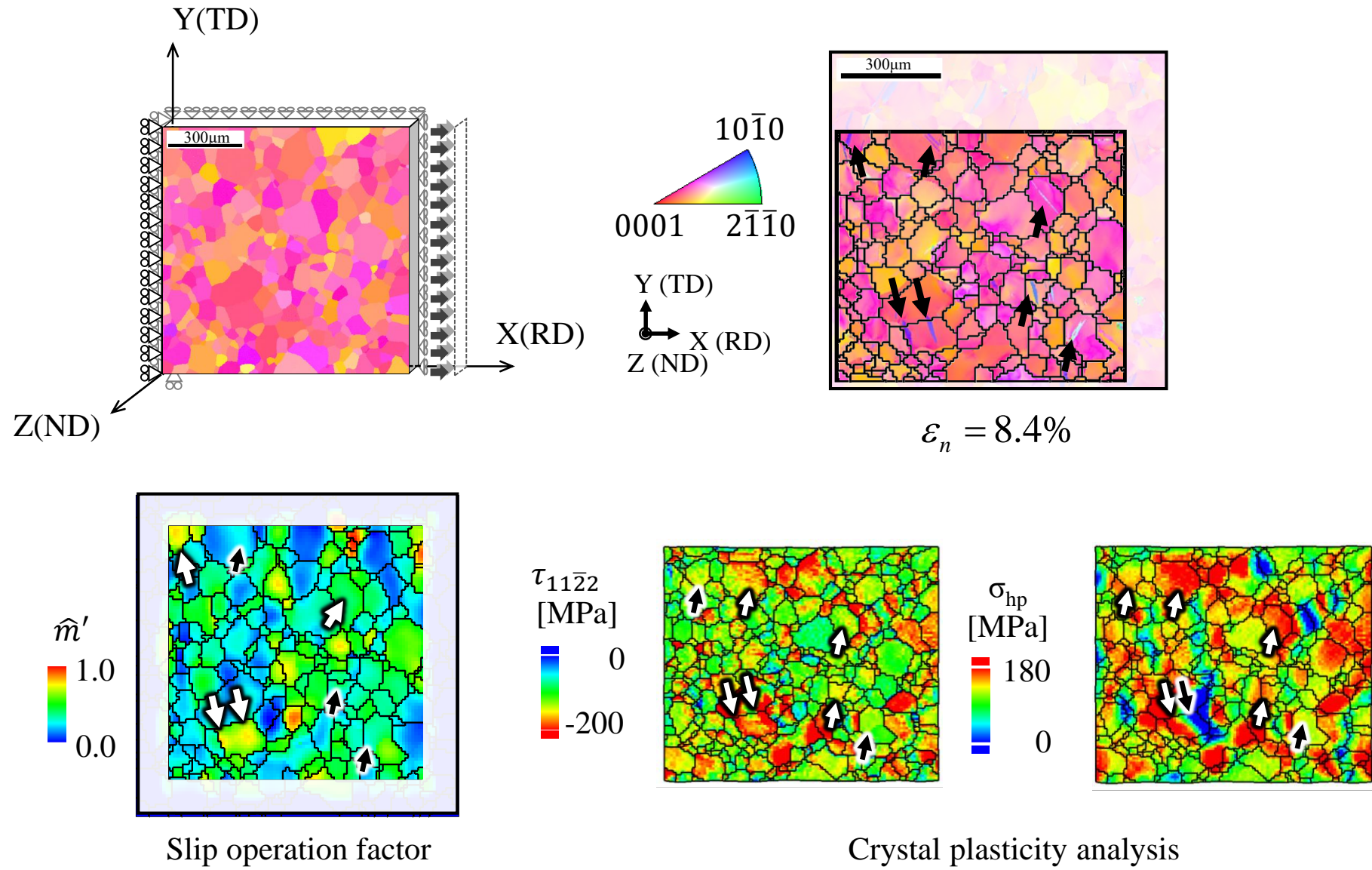
Fig. 1 Geometry of the CP-Ti specimen (a), the EBSD orientation map plotted for the ND (b), and the (0001) pole figure (c).
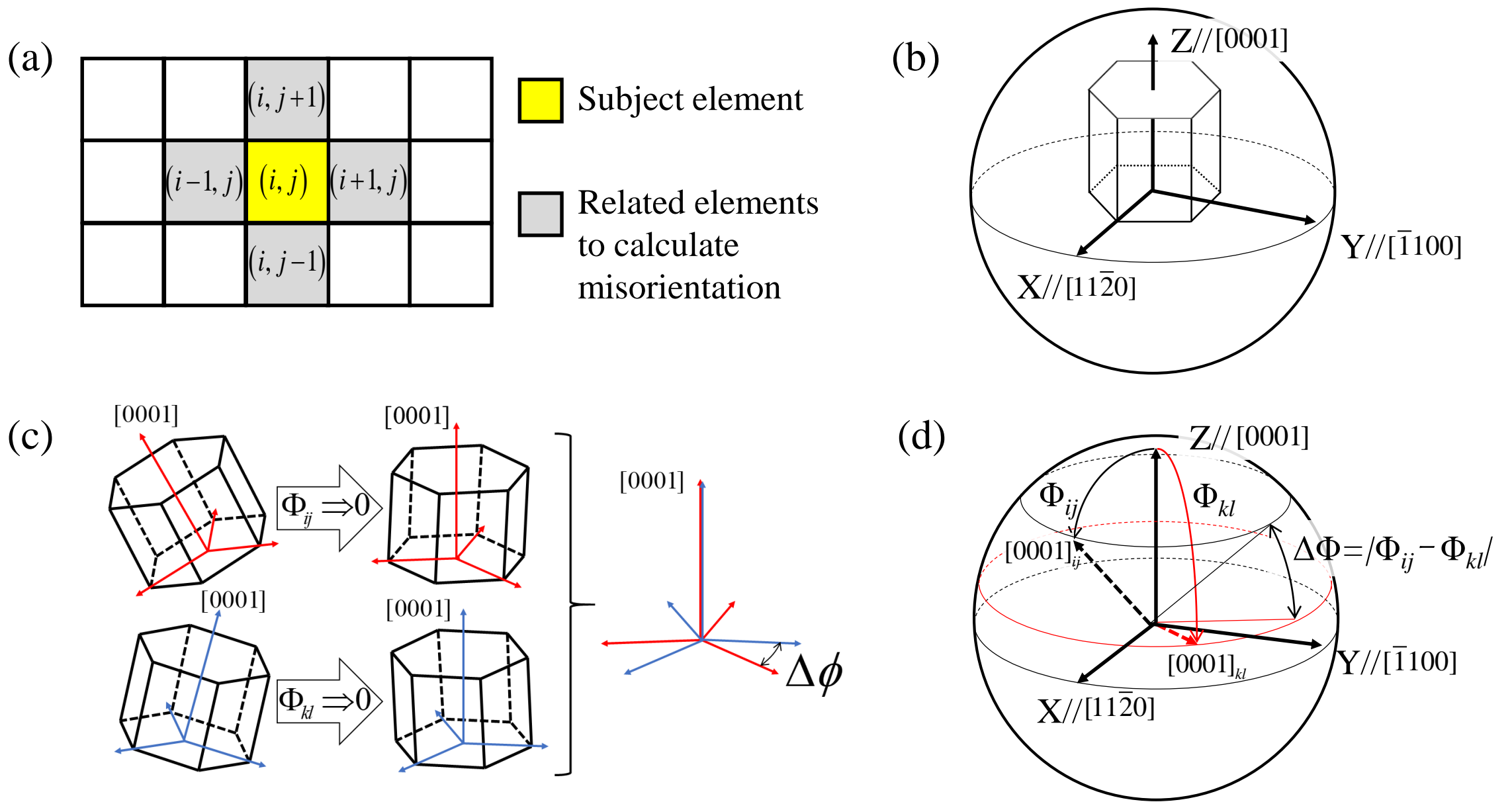
Fig. 2 Schematic of the calculation method of the local misorientation angle. (a) Relationship between address and elements when the microstructural map is divided into rectangular solid elements. (b) Crystal lattice coordinate system when the Euler angles $(\phi_1, \Phi, \phi_2) = (0,0,0)$. Calculation method of misorientation angle around [0001] axis (c) and of [0001] axes (d) between positions (i, j) and (k, l).
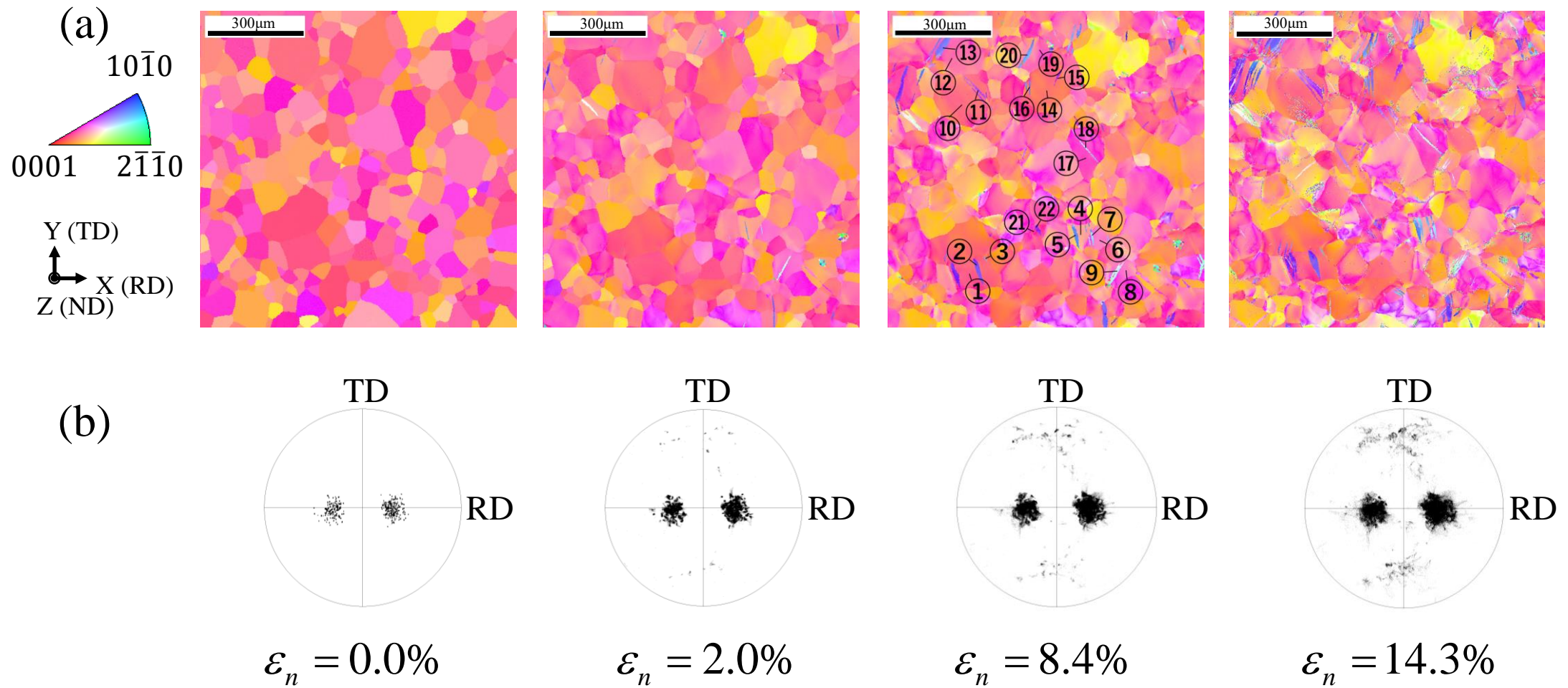
Fig. 3 Changes in EBSD orientation map plotted for the ND (a) and (0001) pole figures (b) under uniaxial tension.

(a)

Bsl<a>   Pri<a>   Pyr1<a>   Pyr1<c+a>   2nd-Pyr<c+a>
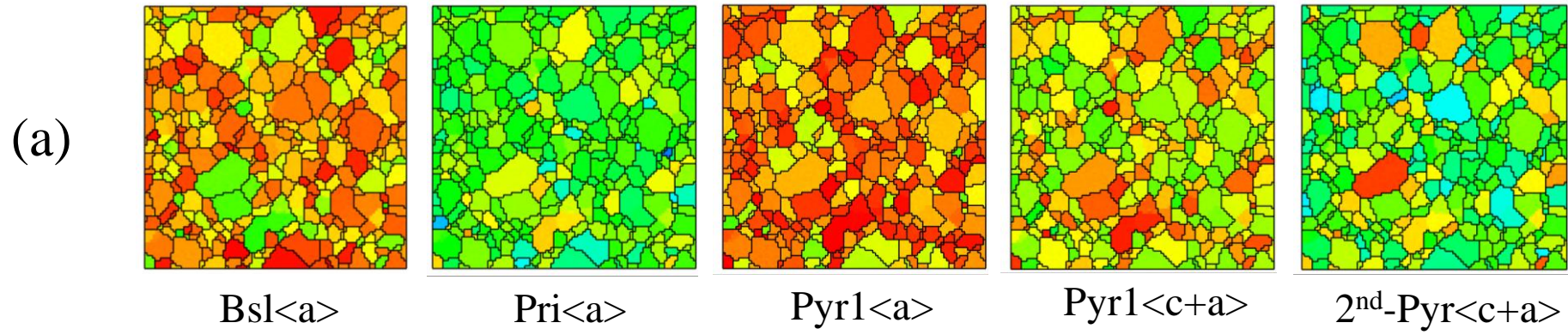
Schmid factor of slip systems in X-direction

(b)

S.F.
0.50

Y (TD)

0.12   Z (ND)   X (RD)

X direction   Y direction   Z direction

$\{10\bar{1}2\}\langle\bar{1}011\rangle$ tension twin $\{11\bar{2}2\}\langle11\bar{2}\bar{3}\rangle$ compression twin
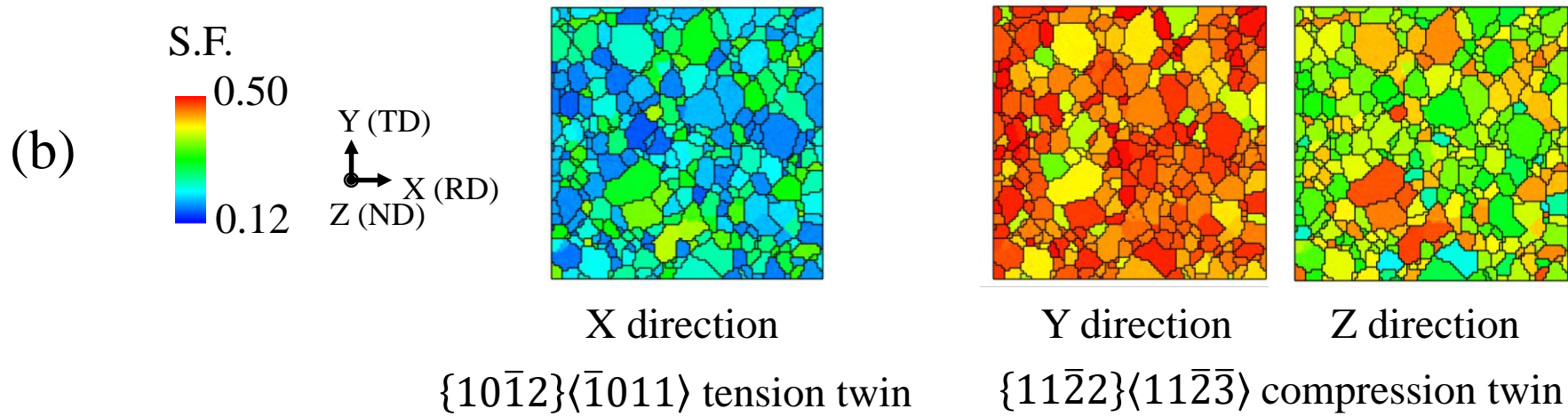
Fig. 4 Distributions of Schmid factors of slip systems (a), and twin systems (b).
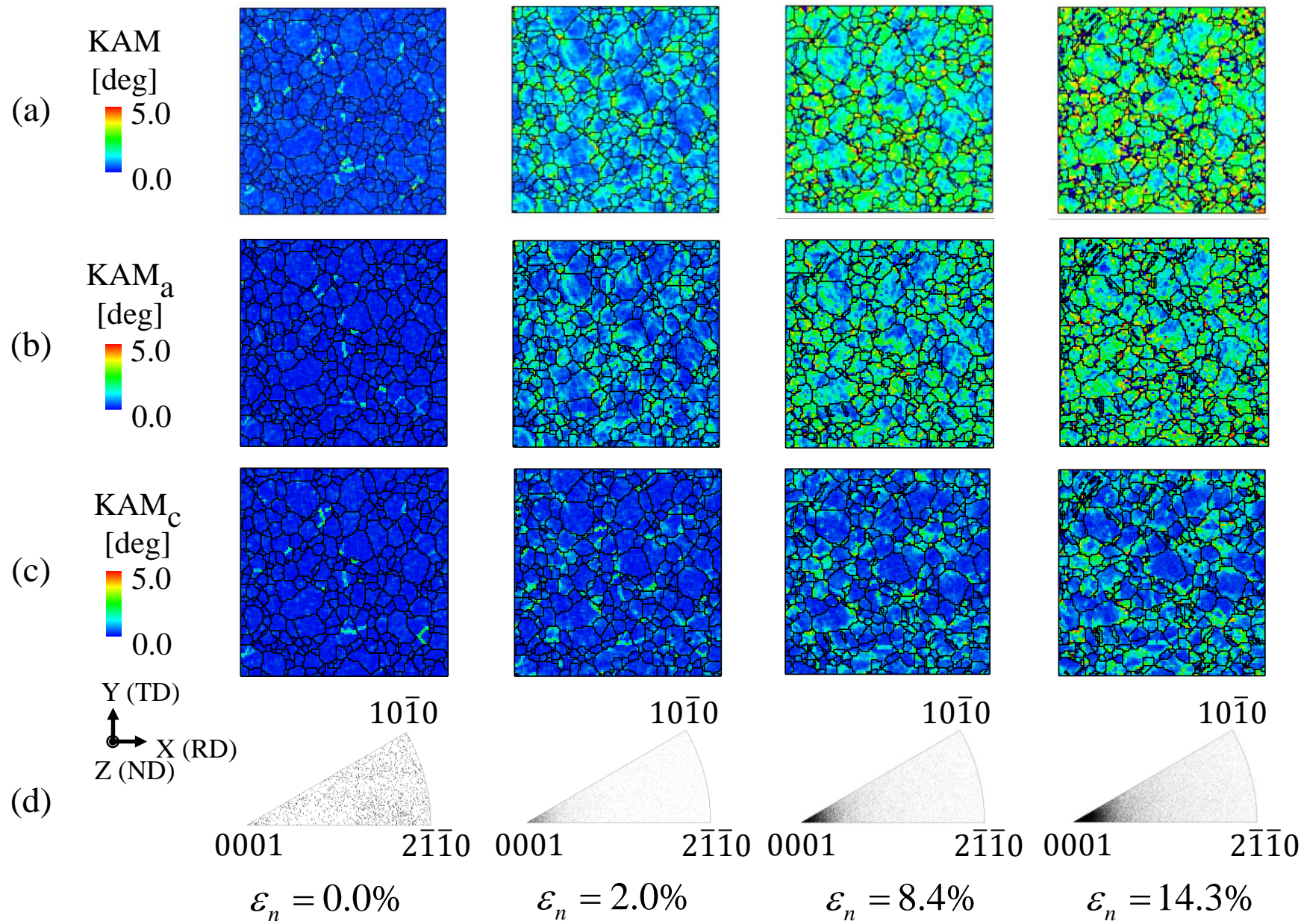
Fig. 5 Development of KAM distributions (a-c) and in-grain misorientation axis (IGMA) (d) under uniaxial tensile deformation. KAM calculated from difference of angles $\Delta\theta$ (Eq. 2) (a), misorientation angles $\Delta\phi$ around [0001] axis (b), and difference of inclination angles $\Delta\Phi$ of [0001] axes (c). IGMA with misorientation angles $\leqq$ $2°$ are plotted in the pole figures (d).
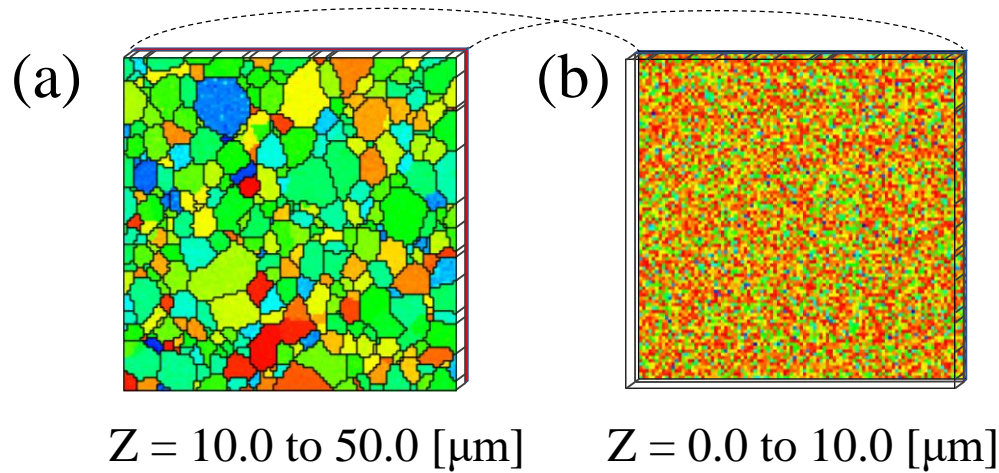
Double layer model

Size:
  1000.0 × 999.4 × 50.0 [μm³]
Elements:
  100 × 100 × 5

Single layer model

Size:
  1000.0 × 999.4 × 20.0 [μm³]
Elements:
  100 × 100 × 2

(a) Z = 10.0 to 50.0 [μm]

(b) Z = 0.0 to 10.0 [μm]
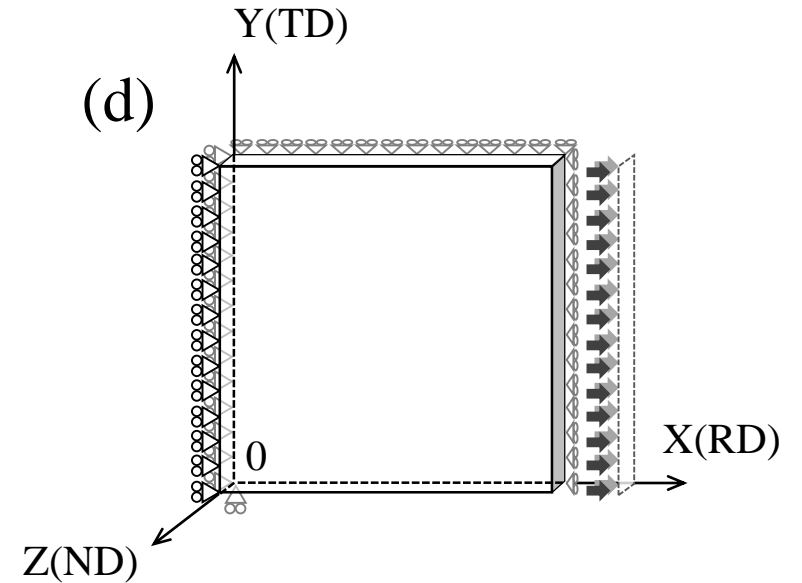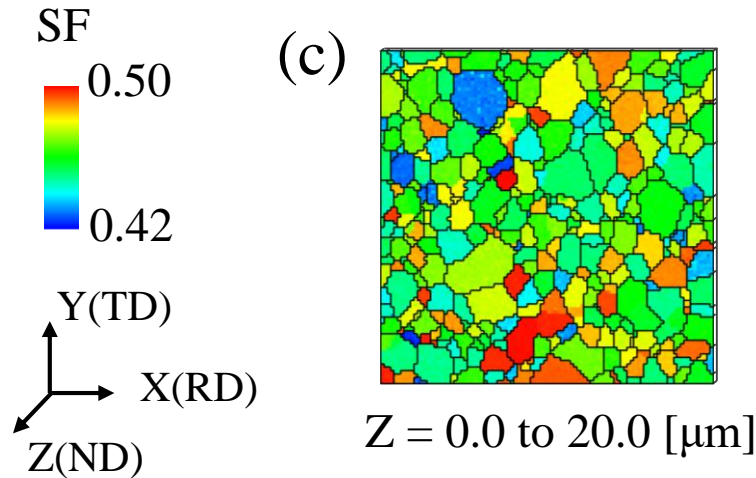
(c) Z = 0.0 to 20.0 [μm]

SF
0.50
0.42

Fig. 6 Vertical cross-sectional views of the geometric models (a-c) and the boundary conditions (d) for the uniaxial tensile analysis. The models were built based on Fig.1a using EBSD-FEM data conversion procedure developed by Kawano et al. [46], and the crystal orientations reflect the inverse pole figure while the crystal orientations in the elements belonging to one layer contacting with the surface at Z = 0.0 μm are randomly given in the double-layer model as shown in the figure (b). The surface at X = 0.0 is fixed in X direction, the surface at Z = 0.0 is fixed in Z direction, and the forced displacement is adapted to the right-hand surface (d). The strain rate is $1.0 \times 10^{-3}\,\mathrm{s}^{-1}$ for all deformation simulations.
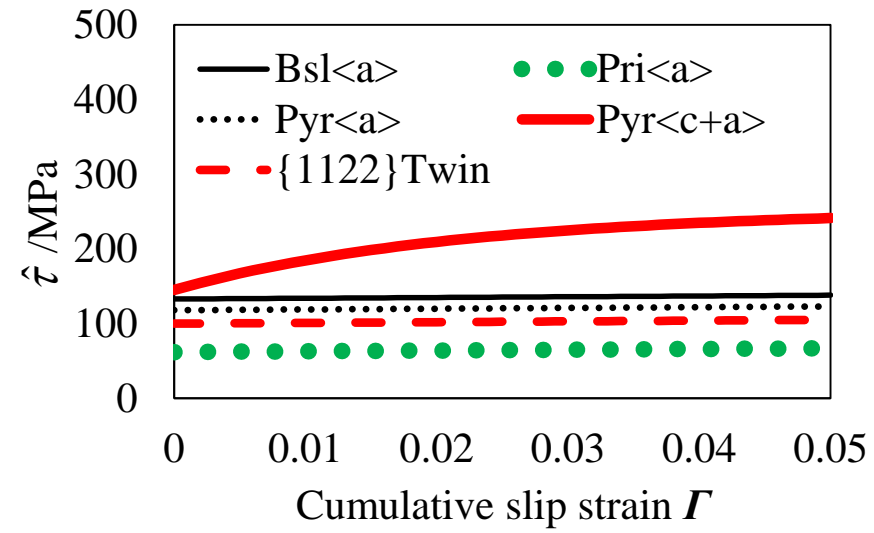
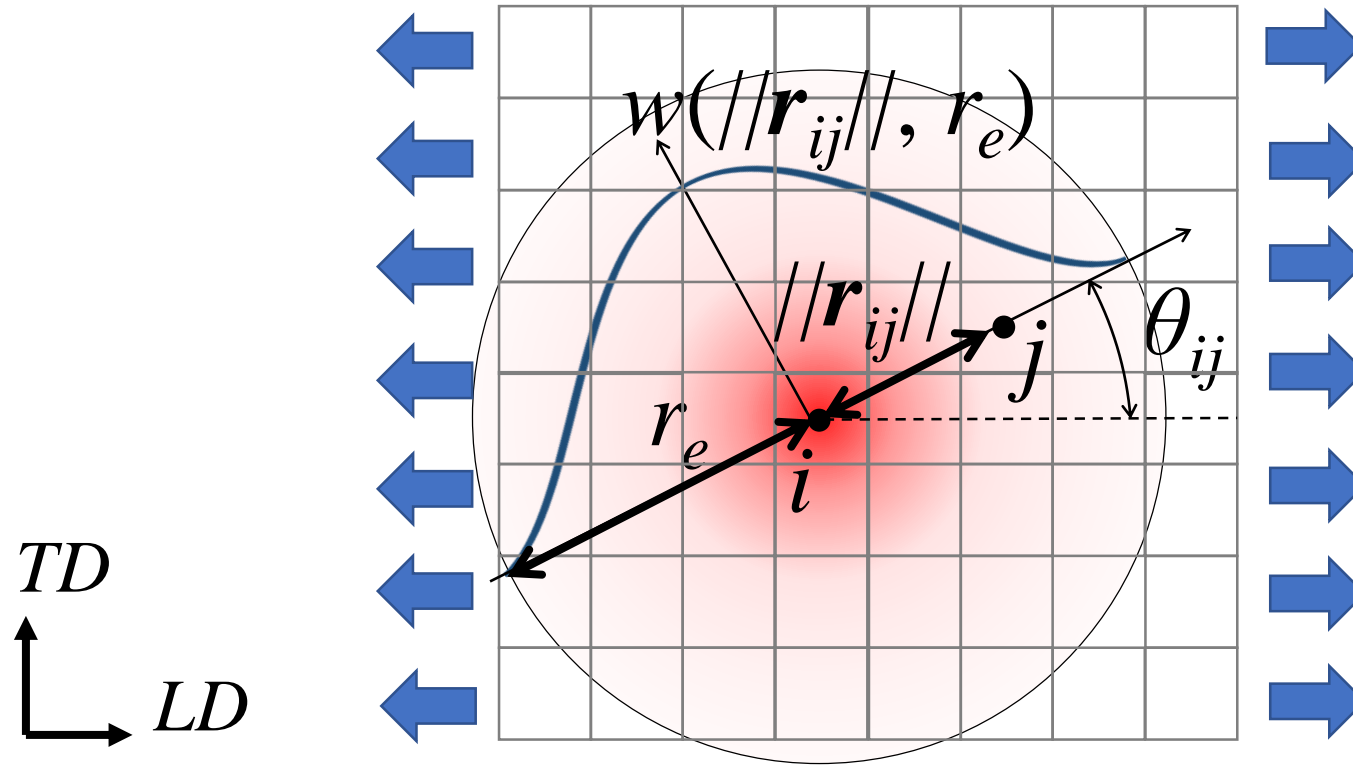Fig. 7 CRSS for each deformation mode as a function of cumulative slip strain.

Fig. 8 CRSS for each deformation mode as a function of cumulative slip strain [32].

Fig. 9 KAM distributions numerically reproduced using the double-layer model. KAM calculated from difference of angles $\Delta\theta$ (Eq. 2) (a), misorientation angles $\Delta\phi$ around [0001] axis (b), and difference of inclination angles $\Delta\Phi$ of [0001] axes (c).
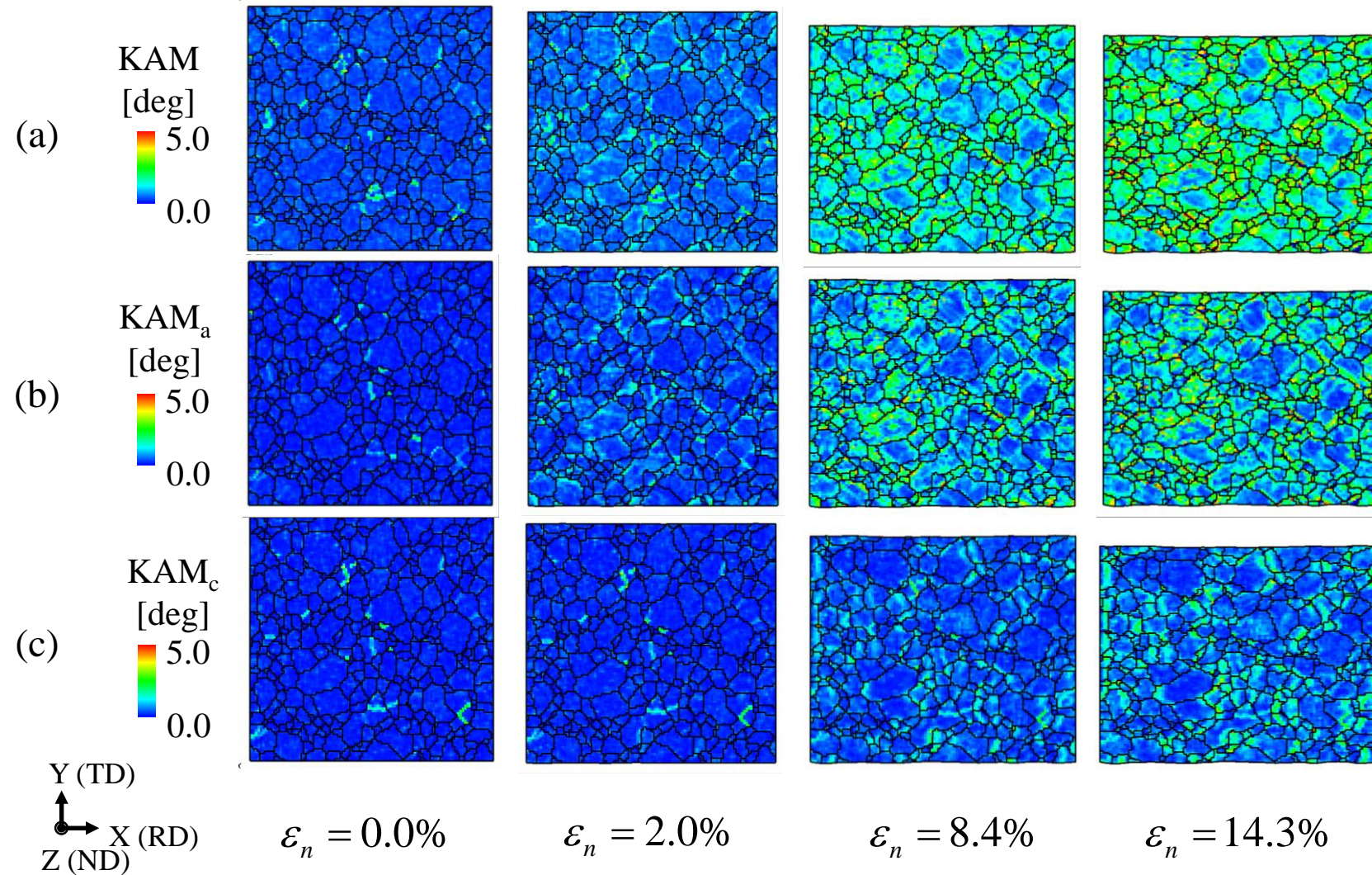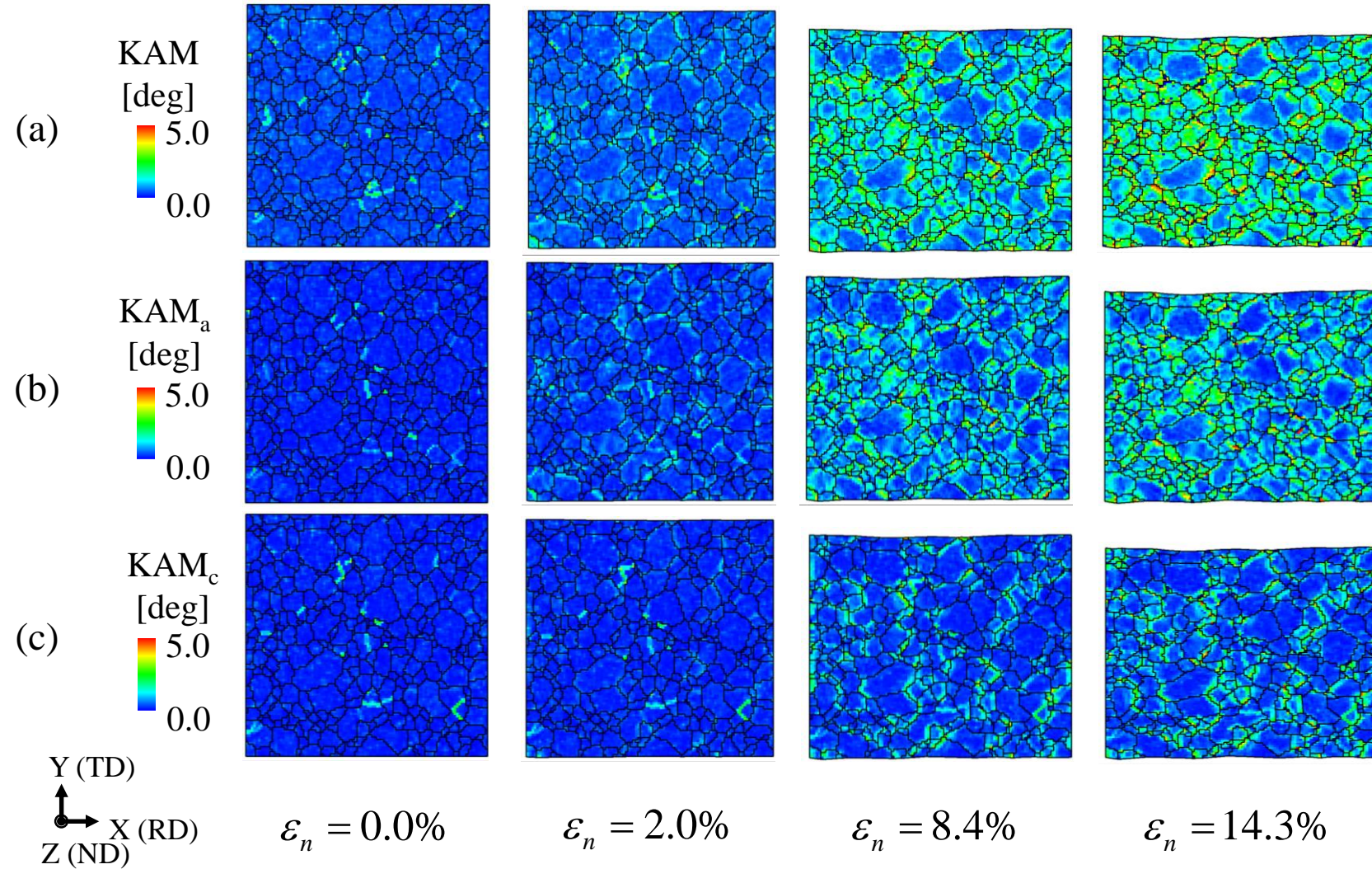
Fig. 10 KAM distributions numerically reproduced using the single-layer model. KAM calculated from difference of angles $\Delta\theta$ (Eq. 2) (a), misorientation angles $\Delta\phi$ around [0001] axis (b), and difference of inclination angles $\Delta\Phi$ of [0001] axes (c).
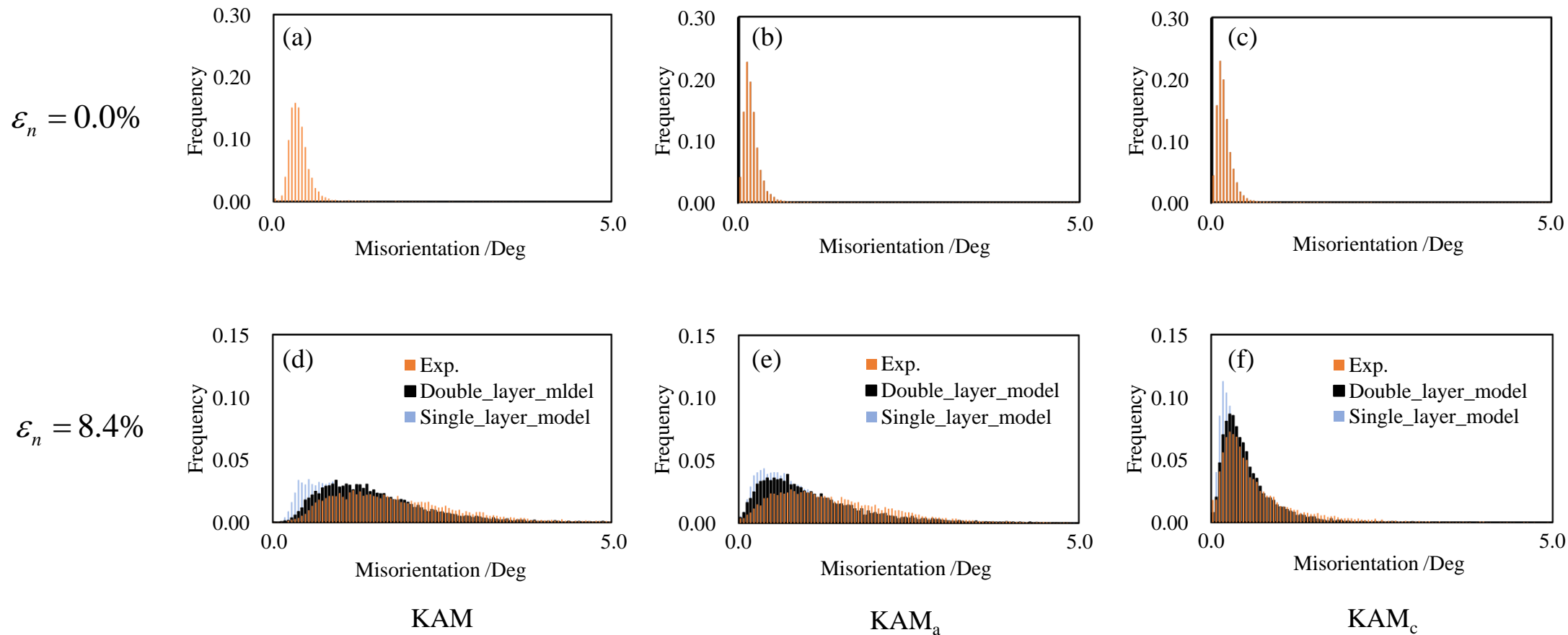
Fig. 11 Frequency distributions of KAM, KAM_a, and KAM_c at $\varepsilon_n = 0.0$ % (a-c) and 8.4 % (d-f). The distributions at the initial state ($\varepsilon_n = 0.0$ %) are the same among those in the experiment (Exp.), double-layer model, and single-layer model.

Fig. 12 Strain distributions obtained by CPFE analysis employing (a) double and (b) single layer model. (c) SOF distributions for the X-directional tension. In the SOF distributions, measuring 2Dave from the outsides were strongly affected by boundary conditions, and they removed from four sides of the models.

(a)

300μm

$10\bar{1}0$

0001 $2\bar{1}\bar{1}0$

Y (TD)

X (RD)
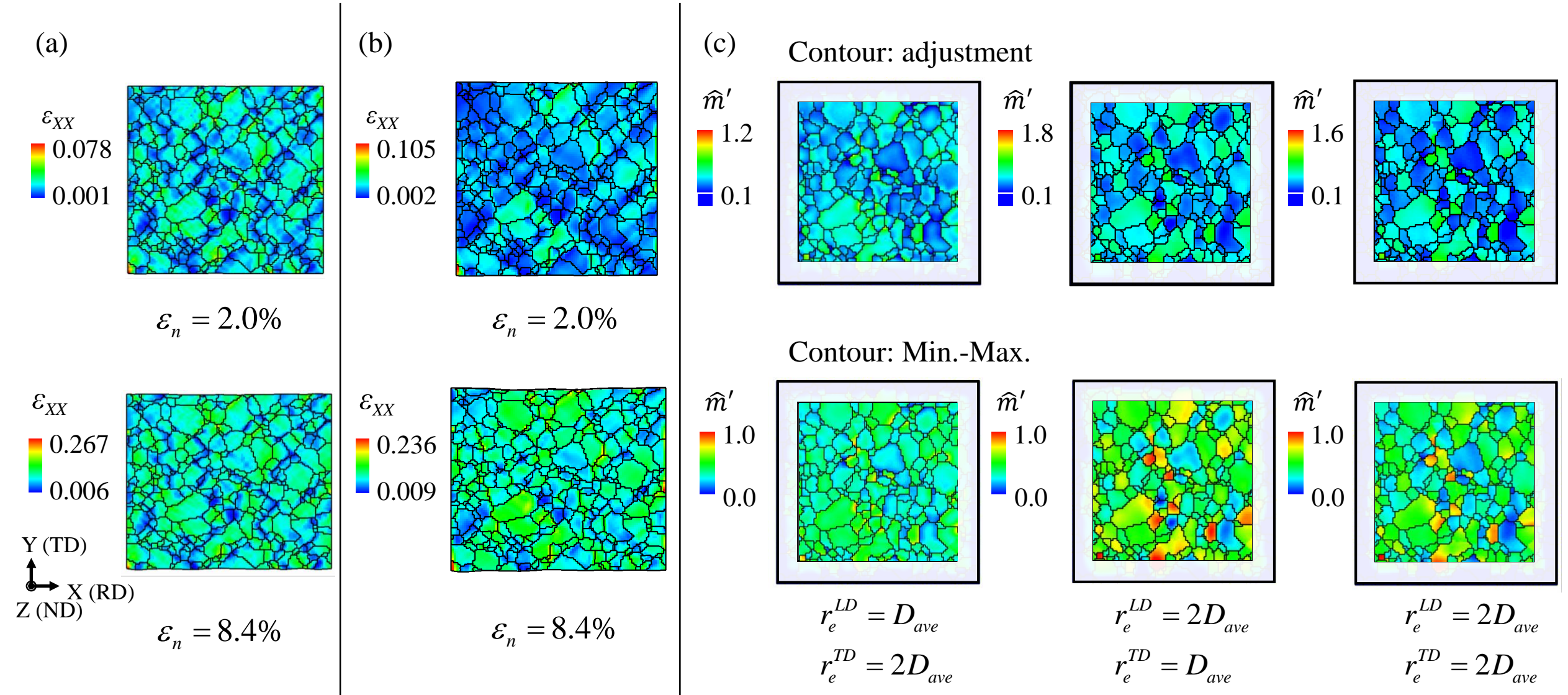Z (ND)

$\varepsilon_n = 8.4\%$

(b)

$\hat{m}'$

1.0

0.0

$r_e^{LD} = D_{ave}$ $r_e^{TD} = 2D_{ave}$

(c)

$r_e^{LD} = 2D_{ave}$ $r_e^{TD} = D_{ave}$

(d)

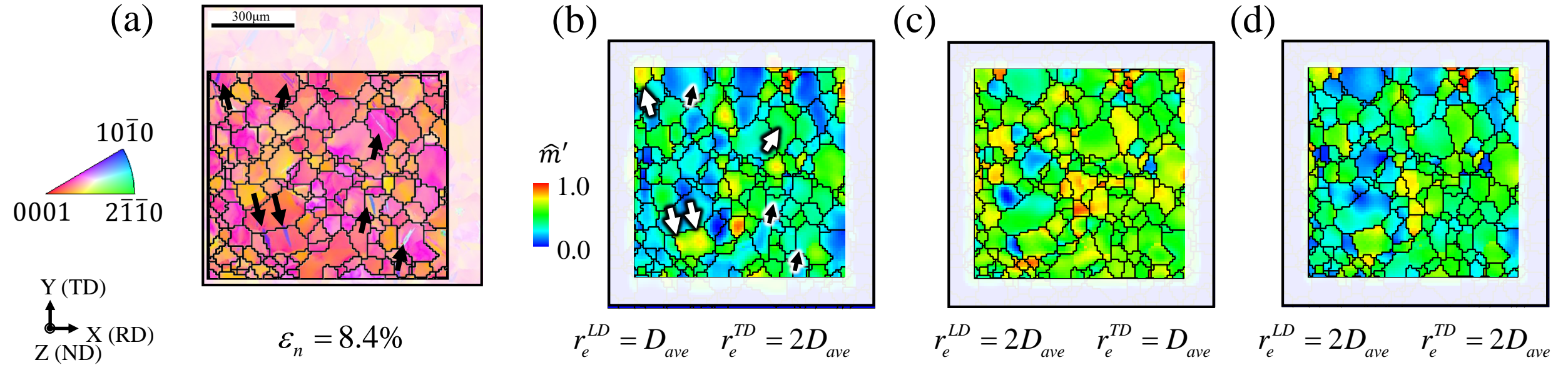$r_e^{LD} = 2D_{ave}$ $r_e^{TD} = 2D_{ave}$

Fig. 13 Comparison of twinning positions. The inverse pole figure obtained by the experiment when the nominal strain is 8.4 % (a) and distributions of SOF for Y-direction for   twin (b-d). Arrows in the figures indicate twin positions. The white arrows in the figure (b) show the successfully predicted twin positions by SOF.

$A^{LD} = 5.0$ $A^{TD} = 5.0$

(a)

$\widehat{m}'$

1.0

0.0

$r_e^{LD} = D_{ave}$ $r_e^{TD} = 2D_{ave}$

(b)

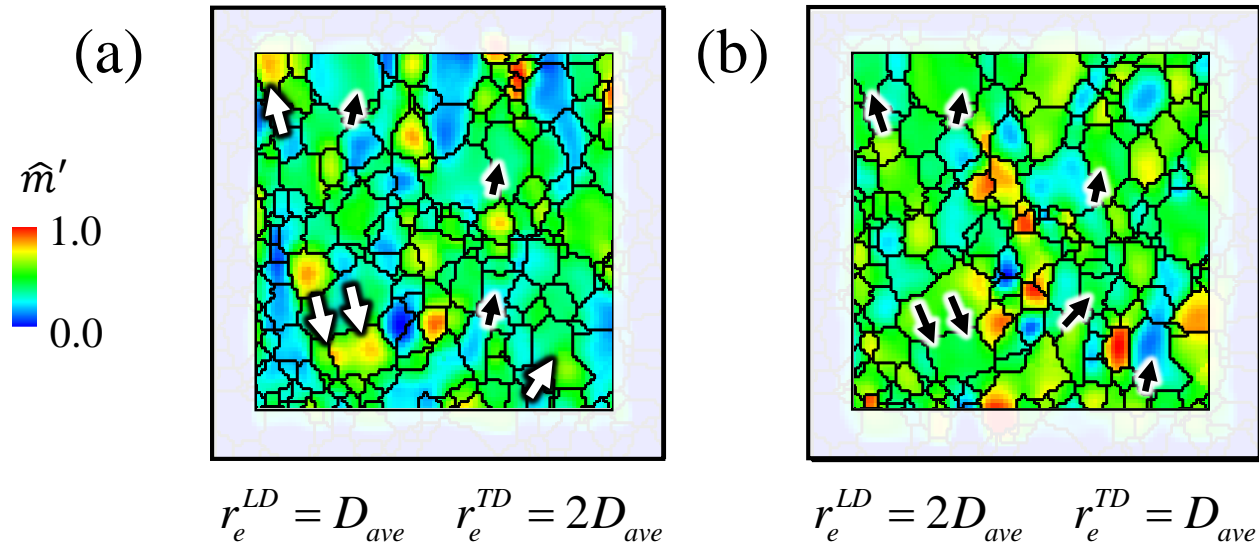$r_e^{LD} = 2D_{ave}$ $r_e^{TD} = D_{ave}$

Fig. 14 SOF distributions for twin when effect of mechanical interactions between regions are strong. Regions indicated by arrows are twinning positions observed in the experiment. The white arrows in the figures show the successfully predicted twin positions by SOF.

$\varepsilon_n = 0.1\%$

(a) σ_{XX} [MPa]

123

89

(b) $\tau_{11\bar{2}2}$ [MPa]

-9

-61

(c) σ_{hp} [MPa]

42

0

$\varepsilon_n = 8.4\%$

(d) σ_{XX} [MPa]

527

-197

(e) $\tau_{11\bar{2}2}$ [MPa]

0

-200

(f) σ_{hp} [MPa]

180

0

Y (TD)
X (RD)
Z (ND)
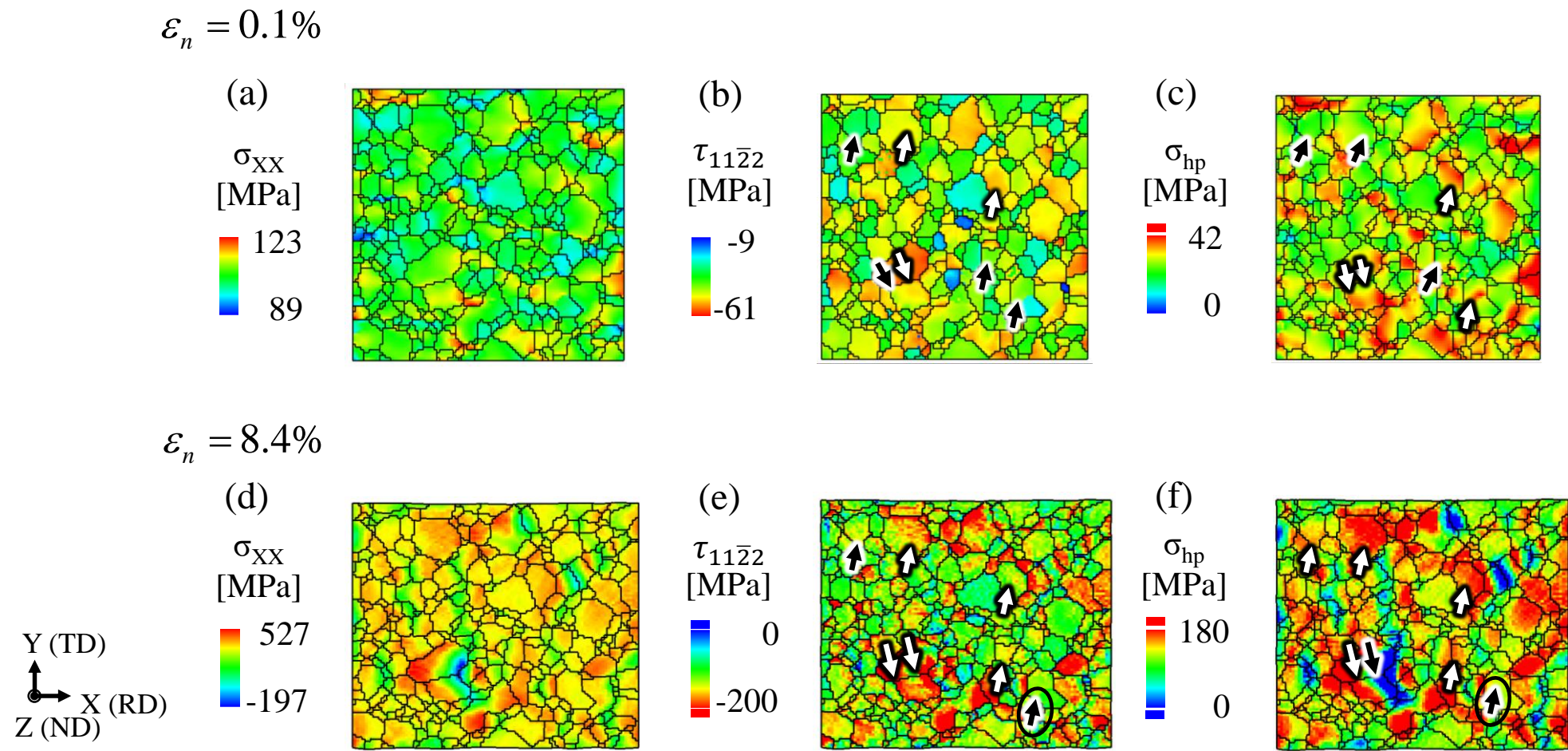
Fig. 15 Stress distributions obtained by CPFE analysis using the double-layer model. (a-c) elastic range and (d-f) plastic range. (a,d) normal stress in the tensile direction (σ_{XX}), (b,e) resolved shear stress for $\{11\bar{2}2\}$ twin ($\tau_{11\bar{2}2}$), and (c,f) hydrostatic pressure (σ^{hp}). Color counters for $\tau_{11\bar{2}2}$ and σ^{hp} are adjusted to observe high stress regions easily. Arrows in the figures indicate twin positions. Successfully predicted twin positions by higher stresses are indicated by white arrows in the figures.

16

Table 1 Chemical composition of the sample material [wt.%].

Ti	O	Fe
Bal.	0.047	0.027

Table 2 Difference of <0001> axes between matrix and twin and estimated twin types.

Position number	Region type	Eulerian angle [deg]			Rotation angle [deg]	Twin type
		ϕ_1	Φ	ϕ_2		
1	Matrix	258.3	27.3	9.7	–	–
2	Twin	188.4	73.3	63.2	66.0	$\{11\bar{2}2\}\langle11\bar{2}\bar{3}\rangle$
3	Twin	293.7	85.8	167.5	64.0	$\{11\bar{2}2\}\langle11\bar{2}\bar{3}\rangle$
4	Matrix	267.6	39.7	16.2	–	–
5	Twin	206.1	82.2	53.1	66.0	$\{11\bar{2}2\}\langle11\bar{2}\bar{3}\rangle$
6	Matrix	277.4	42.3	8.5	–	–
7	Twin	30.3	104.1	313.2	64.3	$\{11\bar{2}2\}\langle11\bar{2}\bar{3}\rangle$
8	Matrix	270.8	41.6	8.2	–	–
9	Twin	168.4	113	46.2	64.9	$\{11\bar{2}2\}\langle11\bar{2}\bar{3}\rangle$
10	Matrix	155.9	151.7	255.1	–	–
11	Twin	164.8	119.1	242.6	33.1	$\{11\bar{2}1\}\langle11\bar{2}\bar{6}\rangle$
12	Matrix	111.9	34.8	380.9	–	–
13	Twin	0.9	106.1	354.5	64.9	$\{11\bar{2}2\}\langle11\bar{2}\bar{3}\rangle$
14	Matrix	89.2	154.6	144.3	–	–
15	Twin	24.7	104.6	355.1	66.0	$\{11\bar{2}2\}\langle11\bar{2}\bar{3}\rangle$
16	Twin	2.4	60.2	179	64.6	$\{11\bar{2}2\}\langle11\bar{2}\bar{3}\rangle$
17	Matrix	254.4	142.7	242.6	–	–
18	Twin	356.5	67.4	167.4	65.0	$\{11\bar{2}2\}\langle11\bar{2}\bar{3}\rangle$
19	Matrix	107.1	37.4	111.1	–	–
20	Twin	351.3	100.7	170.8	66.0	$\{11\bar{2}2\}\langle11\bar{2}\bar{3}\rangle$
21	Matrix	265.8	28.2	358.5	–	–
22	Twin	6.5	112.2	359.6	65.5	$\{11\bar{2}2\}\langle11\bar{2}\bar{3}\rangle$

Table 3 Twinning systems in α-Ti [62].

Twin systems	Rotation axis	Rotation angle [deg]	Twin type
$\{11\bar{2}1\}\langle11\bar{2}\bar{6}\rangle$	$\langle10\bar{1}0\rangle$	35.10	Tension
$\{10\bar{1}1\}\langle10\bar{1}\bar{2}\rangle$	$\langle11\bar{2}0\rangle$	57.42	Compression
$\{11\bar{2}2\}\langle11\bar{2}\bar{3}\rangle$	$\langle10\bar{1}0\rangle$	64.62	Compression
$\{11\bar{2}4\}\langle22\bar{4}\bar{3}\rangle$	$\langle10\bar{1}0\rangle$	76.66	Compression
$\{10\bar{1}2\}\langle10\bar{1}\bar{1}\rangle$	$\langle11\bar{2}0\rangle$	84.78	Tension

Table 4 Elastic compliance of pure titanium [(TPa)-1][63].

s_{11}	s_{12}	s_{13}	s_{33}	s_{44}
9.581	-4.623	-1.893	6.980	21.413

Table 5 Parameters for CPFE analysis and SOF calculation [MPa].

Slip systems	τ_0 (CRSS)	τ_1	θ_0	θ_1
Basal	133.0	100	100	100
Pri<a>	62.0	100	100	100
1st Pyr<a>	118.0	100	100	100
1st & 2nd Pyr <c+a>	145.0	100	5000	100
$\{10\bar{1}2\}\langle10\bar{1}\bar{1}\rangle$ twin	-	-	-	-
$\{11\bar{2}2\}\langle11\bar{2}3\rangle$ twin (for SOF)	100	-	-	-

Table 6 Parameters employed in SOF calculation. D_{ave} (69.2 µm) is an average grain size in the specimen.

CRSSs	Same with τ_0 in Table 5
A^{1st}, A^{2nd}, A^{3rd}, A^{other}	1.0, 1.0, 1.0, 0.0
R_{max}^{LD}, R_{max}^{TD}	5.0, 5.0
A^{LD}, A^{TD}	(i) 1.0, 1.0 (ii) 5.0, 5.0
r_e^{LD}, r_e^{TD}	(i) D_{ave}, $2D_{ave}$ (ii) $2D_{ave}$, D_{ave} (iii) $2D_{ave}$, $2D_{ave}$